Patient-Specific Isogeometric Fluid-Structure Interaction Analysis of Thoracic Aortic Blood Flow due to Implantation of the Jarvik 2000 Left Ventricular Assist Device

Y. Bazilevs [a,1], J. R. Gohean [a,2], T. J. R. Hughes [a,3], R. D. Moser [a,4], and Y. Zhang [b,5]

[a] *Institute for Computational Engineering and Sciences, The University of Texas at Austin, 201 East 24th Street, 1 University Station C0200, Austin, TX 78712, USA*

[b] *Mechanical Engineering, Carnegie Mellon University, Scalfe Hall 303, 5000 Forbes Avenue, Pittsburgh, PA 15213, USA*

Abstract

Left ventricular assist devices (LVADs) are continuous flow pumps that are employed in patients with severe heart failure. Although their emergence has significantly improved therapeutic options for patients with heart failure, detailed studies of the impact of LVADs on hemodynamics are notably lacking. To this end we initiate a computational study of the Jarvik 2000 LVAD model employing isogeometric fluid-structure interaction analysis. We focus on a patient-specific configuration in which the LVAD is implanted in the descending thoracic aorta. We perform computations for three pump settings and report our observations for several quantities of hemodynamic interest.

Key words: arbitrary Lagrangian-Eulerian (ALE) formulation, blood flow, cardiovascular modeling, fluid-structure interaction, hyperelastic solids, incompressible fluids, isogeometric analysis, left ventricular assist devices, mesh movement, moving domains, NURBS, oscillatory shear index, wall shear stress

---

[1] Postoctoral Fellow

[2] Graduate Student. Present affiliation: Windmill Cardiovascular Systems, Inc. Austin, TX

[3] Professor of Aerospace Engineering and Engineering Mechanics, Computational and Applied Mathematics Chair III

[4] Professor of Mechanical Engineering

[5] Assistant Professor

Contents

1 Introduction

Cardiovascular disease is the number one killer of men and women in the US and is the primary cause of congestive heart failure (CHF), which afflicts over 5.2 million Americans. There are 550,000 new cases of CHF reported annually. Cardiovascular diseases produce a number of physiological changes to the tissue of the cardiovascular system (e.g., loss of elasticity of the arteries as in arteriosclerosis, ischemic damage and cardiomyopathies). These change the hemodynamics of the cardiovascular system with potentially disastrous consequences. When other treatments fail,

implanted circulation support devices can be used to reestablish interrupted or inadequate flow. The emergence of axial flow assist devices has significantly advanced therapeutic options for patients with severe heart failure. These devices deliver continuous blood flow and provide distinct advantages with regard to reduction in size, weight, and energy demands, simplified implantation technique, and device control [18].

New, small, efficient non-pulsatile axial flow left ventricle assist devices (LVADs) are currently being studied as bridges to transplant, destination therapy and recovery for CHF. These pumps are highly engineered, optimized devices, but the design of their most effective implant configurations and operating conditions has been more difficult. This is unfortunate because LVADs greatly alter the hemodynamics of the heart and aorta, which can be either helpful, as intended, or harmful, leading to significant complications. Tools to optimize LVAD device design and placement are notably lacking, though both have a significant effect on hemodynamics. Of particular concern regarding hemodynamics is the occurrence of regions in which the blood is stagnant, thought to be a key factor leading to thrombogenesis [53]. Flow stasis was seen clinically using trans-esophageal echo technology in patients with the pump outlet graft in the descending aorta and the LVAD on high speed. Stasis or mild wall shear stress has been correlated with thrombotic events [32].

In this work we perform fluid-structure numerical simulation of a patient-specific model of the aorta, from the aortic valve to the descending thoracic aorta, including flow into branch vessels, and include the effect of the LVAD. The effect of an LVAD on hemodynamics is complex and demands a locally three-dimensional model of the flow in the aortic valve and aorta. We focus on this section of the aorta because this is the region in which the hemodynamics are most affected by the introduction of an LVAD. It is also the region in which hemodynamics has the greatest effect on the health of the heart. Our modeling and simulation efforts are motivated by ongoing clinical studies, which suggest that it is the gross features of the configuration and operating conditions of the device that are in most need of assessment and optimization [26].

For this study we constructed a patient-specific model of the thoracic aorta with an added LVAD branch in the descending location. We consider three different flow conditions: 1) LVAD is off and all the blood flow occurs through the aortic root; 2) LVAD is operating in the regime where over one half of the blood supplied to the aorta comes from the pump; 3) LVAD is operating in the regime where nearly all the flow comes from the LVAD. Inflow data for our patient-specific model was obtained from a lumped-parameter closed-loop multiscale model of the cardiovascular system that was developed in [15]. The latter allows for the inclusion of assist devices.

We use NURBS-based isogeometric analysis for geometry modeling and simulation. (See references [5, 9, 22] for the basics of isogeometric analysis and refer-

ences [3, 54] for application of NURBS-based isogeometric analysis to modeling and simulation of fluid-structure interaction applied to vascular flows.) We use numerical procedures developed in [2] with the following modification to the coupled system solution strategy: at the nonlinear iteration stage we omit the so-called shape derivatives from the left-hand-side tangent matrix, resulting in a simplified coupled solution procedure. No significant influence of this on the nonlinear convergence was observed.

The paper is organized as follows. In Section 2 we present the coupled fluid-structure interaction formulation of vascular blood flow at the continuous level. In this formulation, the blood is modeled as an incompressible viscous fluid and the arterial wall is modeled as a hyperelastic solid. The formulation allows for large structural motions. In Section 3 the semi-discrete formulation of the coupled problem is given and the algorithm to advance the fluid-structure equations in time is described. In Section 4 we present the setup and numerical results of the simulation of blood flow and arterial wall motion in the model of a patient-specific thoracic aorta with LVAD implanted in the descending location. We give a detailed discussion of imposition of initial and boundary conditions. In particular, we present a stable modification of the outflow boundary condition to account for possible cases of locally reversed flow through outflow boundaries. Numerical results obtained for the descending aortic distal anastomosis are in agreement with clinical observations and findings for this configuration. In Section 5, we draw conclusions and outline future research directions.

2   Variational formulation of the coupled fluid-structure interaction problem at the continuous level

In this section we formulate the coupled fluid-structure interaction problem at the continuous level. The current section is a shorter summary of significantly more detailed developments in [2].

2.1   Preliminaries

Let $\Omega_0 \subset \mathbb{R}^d$, $d = 2, 3$, represent the combined fluid (blood) and solid (arterial wall) domain in the initial configuration, which serves simultaneously as the reference configuration. Let $\Omega_t \subset \mathbb{R}^d$ denote a configuration of Ω_0 at a current time t, namely,

$$\Omega_t = \{\boldsymbol{x} \mid \boldsymbol{x} = \hat{\boldsymbol{\phi}}_t(\boldsymbol{y}) \ \forall \ \boldsymbol{y} \in \Omega_0\}, \tag{1}$$

where the ALE mapping $\hat{\boldsymbol{\phi}}_t : \ \Omega_0 \ \rightarrow \ \Omega_t$ denotes the motion of the fluid-solid domain. We label with $\boldsymbol{y}$ and $\boldsymbol{x}$ coordinates in Ω_0 and Ω_t, respectively. We assume
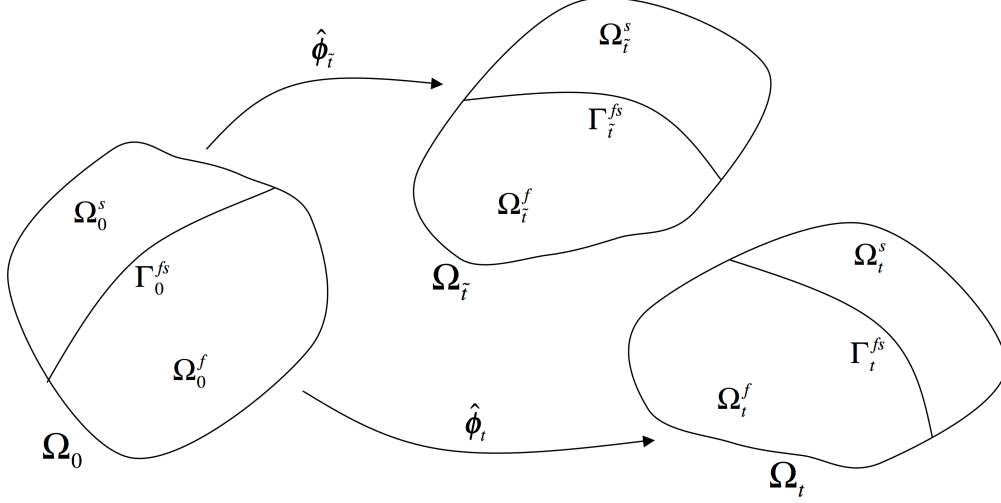
4

Fig. 1. Abstract setting for the fluid-structure interaction problem. Depiction of the initial, the "nearby", and the current configurations related through the ALE mapping. The initial configuration also serves as the reference configuration.

the mapping $\hat{\boldsymbol{\phi}}_t$ is invertible and denote by $\hat{\boldsymbol{\phi}}_t^{-1} : \Omega_t \to \Omega_0$ its inverse.

Give the current time time t, we take $\tilde{t} < t$, and denote by $\Omega_{\tilde{t}}$ a configuration of Ω_0 at time $\tilde{t}$, namely

$$\Omega_{\tilde{t}} = \{\tilde{\boldsymbol{x}} \mid \tilde{\boldsymbol{x}} = \hat{\boldsymbol{\phi}}_{\tilde{t}}(\boldsymbol{y}) \ \forall \ \boldsymbol{y} \in \Omega_0\}. \tag{2}$$

We think of $\Omega_{\tilde{t}}$ as a configuration "nearby" Ω_t that in numerical calculations represents the final configuration at the previous time step. We label with $\tilde{\boldsymbol{x}}$ coordinates in $\Omega_{\tilde{t}}$.

The domain Ω_0 admits the decomposition

$$\Omega_0 = \overline{\Omega_0^f \cup \Omega_0^s}, \tag{3}$$

where Ω_0^f is the subset of Ω_0 occupied by the fluid, and Ω_0^s is the subset of Ω_0 occupied by the solid. The decomposition is non-overlapping, that is

$$\Omega_0^f \cap \Omega_0^s = \emptyset. \tag{4}$$

Likewise,

$$\Omega_t = \overline{\Omega_t^f \cup \Omega_t^s}, \tag{5}$$

with

$$\Omega_t^f \cap \Omega_t^s = \emptyset, \tag{6}$$

5

and

$$\Omega_{\tilde{t}} = \overline{\Omega_{\tilde{t}}^f \cup \Omega_{\tilde{t}}^s}, \tag{7}$$

with

$$\Omega_{\tilde{t}}^f \cap \Omega_{\tilde{t}}^s = \emptyset, \tag{8}$$

Let Γ_0^{fs} denote the interface between the fluid and the solid regions in the initial configuration, and, analogously, let Γ_t^{fs} and $\Gamma_{\tilde{t}}^{fs}$ be its counterpart in the current and "nearby" configurations, respectively. A diagram depicting the configurations and the relationship between them is shown in Figure 1.

The material or Lagrangian description is adopted for the solid. To this end, we set $\boldsymbol{y} = \boldsymbol{X} \in \Omega_0^s$, a "particle" in the material domain, $\hat{\boldsymbol{\phi}}_t(\boldsymbol{y}) = \boldsymbol{\phi}_t(\boldsymbol{X})$ the mapping of the material domain, and use $\boldsymbol{X}$ to denote coordinates in Ω_0^s. In contrast to the solid domain, the motion of the fluid domain is not the particle motion of the fluid. It does, however, conform to the particle motion of the solid at the fluid-solid interface.

2.2 The solid problem

This section gives a weak formulation of the solid in the Lagrangian description. Let $\boldsymbol{u}$ denote the displacement of the solid with respect to the initial configuration,

$$\boldsymbol{u}(\boldsymbol{X}, t) = \boldsymbol{\phi}_t(\boldsymbol{X}) - \boldsymbol{X} \ \forall \ \boldsymbol{X} \in \Omega_0^s, \tag{9}$$

and let $\boldsymbol{w}^s$ be the weighting function for the linear momentum equation. We assume that the displacement satisfies the boundary condition, $\boldsymbol{u} = \boldsymbol{g}^s$ on $\Gamma_0^{s,D}$, the Dirichlet part of the solid domain boundary. We also assume that $\boldsymbol{w}^s = \boldsymbol{0}$ on $\Gamma_0^{s,D}$. Let $\mathcal{V}^s = \mathcal{V}^s(\Omega_0^s)$ denote the trial solution space for displacements and let $\mathcal{W}^s = \mathcal{W}^s(\Omega_0^s)$ denote the trial weighting space for the linear momentum equations. Dirichlet boundary conditions on $\boldsymbol{u}$ and $\boldsymbol{w}^s$ are assumed to be built into the respective function spaces. The variational formulation of the solid problem is stated as follows: Find $\boldsymbol{u} \in \mathcal{V}^s$ such that $\forall \boldsymbol{w}^s \in \mathcal{W}^s$,

$$B^s(\boldsymbol{w}^s, \boldsymbol{u}) = F^s(\boldsymbol{w}^s) \tag{10}$$

where

$$B^s(\boldsymbol{w}^s, \boldsymbol{u}) = \left(\boldsymbol{w}^s, \rho_0^s \frac{\partial^2 \boldsymbol{u}}{\partial t^2}|_X\right)_{\Omega_0^s} + (\nabla_X \boldsymbol{w}^s, \boldsymbol{FS})_{\Omega_0^s}, \tag{11}$$

and

$$F^s(\boldsymbol{w}^s) = (\boldsymbol{w}^s, \rho_0^s \boldsymbol{f}^s)_{\Omega_0^s} + (\boldsymbol{w}^s, \boldsymbol{h}^s)_{\Gamma_0^{s,N}}, \tag{12}$$

6

where $\boldsymbol{F}$ is the deformation gradient defined as

$$\boldsymbol{F} = \frac{\partial \phi_t(\boldsymbol{X})}{\partial \boldsymbol{X}}, \tag{13}$$

$\boldsymbol{S}$ is the second Piola-Kirchhoff stress tensor, $\Gamma_0^{s,N}$ is the Neumann part of the solid boundary, $\boldsymbol{h}^s$ is the boundary traction vector, ρ_s^0 is the density of the solid in the initial configuration, $\boldsymbol{f}^s$ is the body force per unit mass, and $(\cdot, \cdot)_\mathcal{D}$ is the L^2 inner product with respect to domain $\mathcal{D}$. The above relations are written over the initial configuration Ω_0^s, which is also the material configuration. The subscript X on the partial derivative operators indicates that the derivatives are taken with respect to the material coordinates $\boldsymbol{X}$. The second partial time derivative in the first term on the right-hand-side of equation (11) is taken with respect to the material coordinate $\boldsymbol{X}$ held fixed.

The details of the constitutive model used in this work are as follows:

$$\boldsymbol{S} = 2\frac{\partial \psi}{\partial \boldsymbol{C}}, \tag{14}$$

$$\boldsymbol{C} = \boldsymbol{F}^T \boldsymbol{F}, \tag{15}$$

$$\psi = \psi_{iso} + \psi_{dil}, \tag{16}$$

$$\psi_{iso} = \frac{1}{2}\mu^s (\mathrm{tr}\overline{\boldsymbol{C}} - 3), \tag{17}$$

$$\psi_{dil} = \frac{1}{2}\kappa^s (\frac{1}{2}(J^2 - 1) - \ln J), \tag{18}$$

$$\overline{\boldsymbol{C}} = \overline{\boldsymbol{F}}^T \overline{\boldsymbol{F}}, \tag{19}$$

$$\overline{\boldsymbol{F}} = J^{-1/3} \boldsymbol{F}, \tag{20}$$

and

$$J = \det \boldsymbol{F}. \tag{21}$$

Equations (14) - (21) describe a generalized neo-Hookean model with penalty (see, e.g., [10, 41]). This constitutive model fulfills all the normalization conditions necessary for well-posedness (see Marsden and Hughes [33], Holzapfel [20]). In particular, the $\ln J$ term in the definition of ψ_{dil} precludes material instabilities for states

of strong compression. Parameters μ^s and κ^s may be determined by the Lamé constants of the linear elastic model, denoted μ^l and λ^l, by considering the case when the current and the reference configurations coincide. Then, by inspection,

$$\mu^s = \mu^l \tag{22}$$

$$\kappa^s = \lambda^l + \frac{2}{3}\mu^l. \tag{23}$$

Thus, μ^s and κ^s are the shear and bulk moduli, respectively.

2.3 Motion of the fluid subdomain problem

This section gives a weak formulation of the motion of the fluid subdomain. Partial differential equations of linear elastostatics subject to Dirichlet boundary conditions coming from the displacements of the solid region are employed to define the arbitrary Lagrangian-Eulerian (ALE) mapping $\hat{\phi}_t(\boldsymbol{y})$ of the fluid domain. In the discrete setting, the fluid subdomain motion problem is referred to as "mesh moving."

Analogously to the solid problem, we define the displacement of the fluid domain as

$$\hat{\boldsymbol{u}}(\boldsymbol{y}, t) = \hat{\phi}_t(\boldsymbol{y}) - \boldsymbol{y} \,\forall\, \boldsymbol{y} \in \Omega_0^f \tag{24}$$

and write $\hat{\boldsymbol{u}}_t(\boldsymbol{y}) = \hat{\boldsymbol{u}}(\boldsymbol{y}, t)$. Note that $\hat{\boldsymbol{u}}_t$ is defined on Ω_0^f and represents the displacement of the reference configuration at time t. We likewise define the displacement of the fluid domain at time $\tilde{t} < t$ as

$$\hat{\boldsymbol{u}}(\boldsymbol{y}, \tilde{t}) = \hat{\phi}_{\tilde{t}}(\boldsymbol{y}) - \boldsymbol{y} \,\forall\, \boldsymbol{y} \in \Omega_0^f \tag{25}$$

and write $\hat{\boldsymbol{u}}_{\tilde{t}}(\boldsymbol{y}) = \hat{\boldsymbol{u}}(\boldsymbol{y}, \tilde{t})$. To determine $\hat{\phi}_t$ we will construct a linear elastic boundary problem for $\hat{\boldsymbol{u}}_t \circ \hat{\phi}_{\tilde{t}}^{-1}$ and utilize

$$\hat{\phi}_t(\boldsymbol{y}) = \hat{\phi}_{\tilde{t}}(\boldsymbol{y}) + \left(\hat{\boldsymbol{u}}_t \circ \hat{\phi}_{\tilde{t}}^{-1}\right)\left(\hat{\phi}_{\tilde{t}}(\boldsymbol{y})\right), \tag{26}$$

where $\hat{\phi}_{\tilde{t}}$ and $\hat{\boldsymbol{u}}_{\tilde{t}}$ are considered known.

Let $\mathcal{V}^m = \mathcal{V}^m(\Omega_{\tilde{t}}^f)$ denote the trial solution space of displacements and let $\mathcal{W}^m = \mathcal{W}^m(\Omega_{\tilde{t}}^f)$ denote the weighting space for the elastic equilibrium equations. As usual, kinematic boundary conditions are built into the definitions of the spaces, namely,

$$\mathcal{V}^m = \{\boldsymbol{u}^m \mid \boldsymbol{u}^m \in \left(H^1(\Omega_{\tilde{t}}^f)\right)^d, \; \boldsymbol{u}^m = \boldsymbol{u}_t \circ \hat{\phi}_{\tilde{t}}^{-1} \text{ on } \Gamma_{\tilde{t}}^{fs}\} \tag{27}$$

$$\mathcal{W}^m = \{\boldsymbol{w}^m \mid \boldsymbol{w}^m \in \left(H^1(\Omega_{\tilde{t}}^f)\right)^d, \; \boldsymbol{w}^m = \boldsymbol{0} \text{ on } \Gamma_{\tilde{t}}^{fs}\} \tag{28}$$

where $\boldsymbol{u}_t$ is the particle displacement at time t. Because $\boldsymbol{u}_t$ is an unknown in our formulation, it will be solved for simultaneously along with $\hat{\boldsymbol{u}}_t$ in a coupled fashion.

The variational formulation of the problem is stated as follows: Find $\hat{\boldsymbol{u}}_t \circ \hat{\boldsymbol{\phi}}_{\tilde{t}}^{-1} \in \mathcal{V}^m$ such that $\forall \boldsymbol{w}^m \in \mathcal{W}^m$,

$$B^m(\boldsymbol{w}^m, \hat{\boldsymbol{u}}_t \circ \hat{\boldsymbol{\phi}}_{\tilde{t}}^{-1}) = F^m(\boldsymbol{w}^m), \tag{29}$$

where

$$B^m(\boldsymbol{w}^m, \boldsymbol{u}^m) = (\nabla_{\tilde{x}}^s \boldsymbol{w}^m, 2\mu^m \nabla_{\tilde{x}}^s \boldsymbol{u}^m)_{\Omega_{\tilde{t}}^f} + (\nabla_{\tilde{x}} \cdot \boldsymbol{w}^m, \lambda^m \nabla_{\tilde{x}} \cdot \boldsymbol{u}^m)_{\Omega_{\tilde{t}}^f}, \tag{30}$$

$$F^m(\boldsymbol{w}^m) = B^m(\boldsymbol{w}^m, \hat{\boldsymbol{u}}_{\tilde{t}} \circ \hat{\boldsymbol{\phi}}_{\tilde{t}}^{-1}), \tag{31}$$

and $\nabla_{\tilde{x}}$ is the gradient operator on $\Omega_{\tilde{t}}$ and $\nabla_{\tilde{x}}^s$ is its symmetrization. The fluid subdomain motion problem may be thought of as a succession of fictitious linear elastic boundary-value problems designed simply to produce a smooth evolution of the fluid mesh. Lamé parameters μ^m and λ^m of the fictitious linear elastic model should be selected such that the fluid mesh quality is preserved for as long as possible. In particular, mesh quality can be preserved by dividing the elastic coefficients by the Jacobian determinant of the element mapping, effectively increasing the stiffness of the smaller elements [34, 50], which are typically placed at fluid-solid interfaces. More advanced mesh moving techniques may be found in [42, 43].

The above construction allows us to define the ALE mapping for the entire domain in a piece-wise fashion, namely

$$\hat{\boldsymbol{\phi}}_t(\boldsymbol{y}) = \begin{cases} \boldsymbol{X} + \boldsymbol{u}(\boldsymbol{X}, t) & \forall \boldsymbol{X} \in \Omega_0^s \\ \boldsymbol{y} + \hat{\boldsymbol{u}}(\boldsymbol{y}, t) & \forall \boldsymbol{y} \in \Omega_0^f \end{cases} \tag{32}$$

Note that due to (27), the ALE map $\hat{\boldsymbol{\phi}}$ in (32) is continuous at the fluid-solid interface. The velocity of the fluid domain is obtained by taking a partial time derivative of $\hat{\boldsymbol{u}}$ with $\boldsymbol{y}$ held fixed, that is, $\hat{\boldsymbol{v}} = \partial \hat{\boldsymbol{u}} / \partial t|_y$.

2.4 The fluid problem

In this section we give a weak formulation of the incompressible Navier-Stokes fluid on a moving domain in the ALE description. Motion of the fluid domain was constructed in the previous section. Let $\mathcal{V}^f = \mathcal{V}^f(\Omega_t^f)$ denote the trial solution space of velocities and pressures and let $\mathcal{W}^f = \mathcal{W}^f(\Omega_t^f)$ denote the trial weighting space for the momentum and continuity equations. Let $\{\boldsymbol{v}, p\}$ denote the particle velocity-pressure pair and $\{\boldsymbol{w}^f, q^f\}$ the weighting functions for the momentum and

continuity equations. We also assume that the fluid particle velocity field satisfies the boundary condition, $\boldsymbol{v} = \boldsymbol{g}^f$ on $\Gamma_t^{f,D}$, the Dirichlet part of the fluid boundary. The variational formulation is stated as follows: Find $\{\boldsymbol{v}, p\} \in \mathcal{V}^f$ such that $\forall\{\boldsymbol{w}^f, q^f\} \in \mathcal{W}^f$,

$$B^f(\{\boldsymbol{w}^f, q^f\}, \{\boldsymbol{v}, p\}; \hat{\boldsymbol{v}}) = F^f(\{\boldsymbol{w}^f, q^f\}) \tag{33}$$

where

$$B^f(\{\boldsymbol{w}^f, q^f\}, \{\boldsymbol{v}, p\}; \hat{\boldsymbol{v}}) = \left(\boldsymbol{w}^f, \rho^f \frac{\partial \boldsymbol{v}}{\partial t}|_y\right)_{\Omega_t^f} + \left(\boldsymbol{w}^f, \rho^f (\boldsymbol{v} - \hat{\boldsymbol{v}}) \cdot \nabla_x \boldsymbol{v}\right)_{\Omega_t^f} \tag{34}$$

$$+ (q^f, \nabla_x \cdot \boldsymbol{v})_{\Omega_t^f} - (\nabla_x \cdot \boldsymbol{w}^f, p)_{\Omega_t^f} + \left(\nabla_x^s \boldsymbol{w}^f, 2\mu^f \nabla_x^s \boldsymbol{v}\right)_{\Omega_t^f},$$

and

$$F^f(\{\boldsymbol{w}^f, q^f\}) = (\boldsymbol{w}^f, \rho^f \boldsymbol{f}^f)_{\Omega_t^f} + (\boldsymbol{w}^f, \boldsymbol{h}^f)_{\Gamma_t^{f,N}}, \tag{35}$$

where ∇_x is the gradient operator on Ω_t, ∇_x^s is its symmetrization, $\Gamma_t^{f,N}$ is the Neumann part of the fluid domain boundary, $\boldsymbol{h}^f$ is the boundary traction vector, $\boldsymbol{f}^f$ is the body force per unit mass, and ρ^f and μ^f are the density and the dynamic viscosity of the fluid, respectively. The partial time derivative in the first term on the right-hand-side of equation (34) is taken with respect to the referential coordinate $\boldsymbol{y}$ held fixed.

2.5 The coupled problem

In this section we present the coupled fluid-structure interaction problem, which is based on the individual subproblems introduced previously. The variational formulation for the coupled problem is stated as: Find $\{\boldsymbol{v}, p\} \in \mathcal{V}^f$, $\boldsymbol{u} \in \mathcal{V}^s$, and $\hat{\boldsymbol{u}} \in \mathcal{V}^m$ such that $\forall\{\boldsymbol{w}^f, q^f\} \in \mathcal{W}^f$, $\forall \boldsymbol{w}^s \in \mathcal{W}^s$, and $\forall \boldsymbol{w}^m \in \mathcal{W}^m$,

$$\begin{aligned} B^f(\{\boldsymbol{w}^f, q^f\}, \{\boldsymbol{v}, p\}; \hat{\boldsymbol{v}}) - F^f(\{\boldsymbol{w}^f, q^f\}) + \\ B^s(\boldsymbol{w}^s, \boldsymbol{u}) - F^s(\boldsymbol{w}^s) + B^m(\boldsymbol{w}^m, \hat{\boldsymbol{u}}) - F^m(\boldsymbol{w}^m) = 0. \end{aligned} \tag{36}$$

with the following auxiliary relations holding in the sense of traces:

$$\boldsymbol{v} = \frac{\partial \boldsymbol{u}}{\partial t}|_X \circ \hat{\phi}_t^{-1} \quad \text{on } \Gamma_t^{fs}, \tag{37}$$

$$\boldsymbol{w}^f = \boldsymbol{w}^s \circ \hat{\phi}_t^{-1} \quad \text{on } \Gamma_t^{fs}. \tag{38}$$

Relationship (37), the kinematic constraint, equates the fluid particle velocity with that of the solid at the fluid-solid boundary. Implications of the coupled formulation

(36), together with the compatibility condition (38), are:

$$\mathcal{L}^f(\boldsymbol{v}, p; \hat{\boldsymbol{v}}) - \rho^f \boldsymbol{f}^f = \boldsymbol{0} \quad \text{on } \Omega_t^f, \tag{39}$$

$$\nabla_x \cdot \boldsymbol{v} = 0 \quad \text{on } \Omega_t^f, \tag{40}$$

$$\mathcal{L}^s(\boldsymbol{u}) - \rho_0^s \boldsymbol{f}^s = \boldsymbol{0} \quad \text{on } \Omega_0^s, \tag{41}$$

$$\boldsymbol{\sigma}^f \boldsymbol{n}_t^f + \boldsymbol{\sigma}^s \boldsymbol{n}_t^s = \boldsymbol{0} \quad \text{on } \Gamma_t^{fs}, \tag{42}$$

where

$$\mathcal{L}^f(\boldsymbol{v}, p; \hat{\boldsymbol{v}}) = \rho^f \frac{\partial \boldsymbol{v}}{\partial t}\Big|_y + \rho^f (\boldsymbol{v} - \hat{\boldsymbol{v}}) \cdot \nabla_x \boldsymbol{v} - \nabla_x \cdot \boldsymbol{\sigma}^f, \tag{43}$$

$$\boldsymbol{\sigma}^f = -\nabla_x p \boldsymbol{I} + 2\mu^f \nabla_x^s \boldsymbol{v}, \tag{44}$$

$$\mathcal{L}^s(\boldsymbol{u}) = \rho_0^s \frac{\partial^2 \boldsymbol{u}}{\partial t^2}\Big|_X - \nabla_X \cdot \boldsymbol{P}. \tag{45}$$

$$\boldsymbol{P} = \boldsymbol{F}\boldsymbol{S}, \tag{46}$$

$$\boldsymbol{\sigma}^s = J^{-1} \boldsymbol{P} \boldsymbol{F}^T, \tag{47}$$

and $\boldsymbol{n}_t^f$ and $\boldsymbol{n}_t^s$ are the unit outward normal vectors to the fluid and solid domains in the current configuration. Equations (39) - (42) imply that the fluid and the solid momentum equations and the fluid incompressibility constraint hold in the interior of the appropriate subdomains, and surface tractions are in equilibrium at the fluid-solid interface.

3 Formulation of the fluid-structure interaction problem at the discrete level

In this section we give a formulation of the fluid-structure interaction equation (36) in the discrete setting. We begin by defining the spatial discretization of the problem. It is exactly the same for finite elements and NURBS-based isogeometric analysis. Having defined the semi-discrete forms, we present the time stepping algorithm, which is the generalized-α method [8, 24].

3.1 Approximation spaces for the coupled problem

Let $\hat{N}_A$ denote a set of basis functions that define the discretization of Ω_0 and let I denote their index set. $\hat{N}_A$ are "fixed" in space on the reference domain and thus are time-independent. The discrete ALE mapping, also denoted by $\hat{\phi}_t(\boldsymbol{y})$ for convenience, takes on the form

$$\hat{\phi}_t(\boldsymbol{y}) = \sum_{A \in I} \hat{\phi}_A(t) \hat{N}_A(\boldsymbol{y}) = \sum_{A \in I} (\hat{\boldsymbol{U}}_A(t) + \boldsymbol{y}_A) \hat{N}_A(\boldsymbol{y}) \tag{48}$$

In (48) $\hat{\boldsymbol{U}}_A(t)$'s are the mesh displacement degrees of freedom and $\boldsymbol{y}_A$'s are the control points in isogeometric analysis and nodal coordinates in standard finite elements that define the reference geometry. The mapping (48) pertains to the entire fluid-structure domain. The motion of the fluid subdomain is obtained from (48) by restricting the index set to the fluid control variables (nodal variables in the case of finite elements). We write $I = I_f \cup I_s$, where I_f and I_s are the index sets of the fluid and solid control variables, respectively.

Because the solid problem (10) is posed over the reference configuration with the unknown fields expressed as functions of the material coordinates $\boldsymbol{X}$, we use $\{\hat{N}_A\}_{A \in I_s}$ to approximate the solid displacements in the material domain. On the other hand, the fluid problem (33) is posed over the current configuration with unknown fields expressed as functions of the spatial coordinates $\boldsymbol{x}$. In order to approximate the unknown velocity and pressure fields in the current domain, we employ $\{N_A(\boldsymbol{x}, t) = \hat{N}_A \circ \hat{\boldsymbol{\phi}}_t^{-1}(\boldsymbol{x})\}_{A \in I_f}$. Finally, the mesh motion problem make use of yet another set of basis functions, $\{\tilde{N}_A(\tilde{\boldsymbol{x}}) = \hat{N}_A \circ \hat{\boldsymbol{\phi}}_{\tilde{t}}^{-1}(\boldsymbol{x})\}_{A \in I_f}$, defined over the "nearby" configuration. It is a simple matter to show that the fluid mesh velocity in the current configuration, used in the formulation of the fluid problem, becomes (see [2] for details):

$$\hat{\boldsymbol{v}}(\boldsymbol{x}, t) = \sum_{A \in I_f} \frac{\partial \hat{\boldsymbol{U}}_A}{\partial t}(t) N_A(\boldsymbol{x}, t). \tag{49}$$

We assume that all basis functions in the reference configuration are at least C^0-continuous, which automatically makes them H^1-conforming. In this work, we also require that the discretization at the fluid-solid interface is conforming, that is, $\hat{N}_A$'s are C^0-continuous across Γ_0^{fs}. As a result, by construction, basis functions in all configurations are H^1-conforming and C^0-continuous across the fluid-solid interface.

3.2   The semi-discrete problem

Let $\mathcal{V}_h^f, \mathcal{V}_h^s, \mathcal{V}_h^m$ and $\mathcal{W}_h^f, \mathcal{W}_h^s, \mathcal{W}_h^m$ be the finite dimensional subspaces corresponding to their infinite dimensional counterparts. We approximate the coupled fluid-structure interaction problem (36) as follows: Find $\{\boldsymbol{v}, p\} \in \mathcal{V}_h^f$, $\boldsymbol{u} \in \mathcal{V}_h^s$, and $\hat{\boldsymbol{u}} \in \mathcal{V}_h^m$ such that $\forall \{\boldsymbol{w}^f, q^f\} \in \mathcal{W}_h^f$, $\forall \boldsymbol{w}^s \in \mathcal{W}_h^s$, and $\forall \boldsymbol{w}^m \in \mathcal{W}_h^m$,

$$\begin{aligned} B_{MS}^f(\{\boldsymbol{w}^f, q^f\}, \{\boldsymbol{v}, p\}; \hat{\boldsymbol{v}}) - F_{MS}^f(\{\boldsymbol{w}^f, q^f\}) \\ + B^s(\boldsymbol{w}^s, \boldsymbol{u}) - F^s(\boldsymbol{w}^s) \\ + B^m(\boldsymbol{w}^m, \hat{\boldsymbol{u}}) - F^m(\boldsymbol{w}^m) = 0, \tag{50} \end{aligned}$$

where

$$B^f_{MS}(\{\boldsymbol{w}^f, q^f\}, \{\boldsymbol{v}, p\}; \hat{\boldsymbol{v}}) = B^f(\{\boldsymbol{w}^f, q^f\}, \{\boldsymbol{v}, p\}; \hat{\boldsymbol{v}})$$
$$+ \left((\boldsymbol{v} - \hat{\boldsymbol{v}}) \cdot \nabla_x \boldsymbol{w}^f, \boldsymbol{v}'\right)_{\tilde{\Omega}^f_t} + (\nabla_x q^f, \frac{1}{\rho^f} \boldsymbol{v}')_{\tilde{\Omega}^f_t}$$
$$+ (\nabla_x \cdot \boldsymbol{w}^f \rho^f \tau_C, \nabla_x \cdot \boldsymbol{v})_{\tilde{\Omega}^f_t} - (\boldsymbol{w}^f, \boldsymbol{v}' \cdot \nabla_x \boldsymbol{v})_{\tilde{\Omega}^f_t}$$
$$- (\nabla_x \boldsymbol{w}^f, \frac{1}{\rho^f} \boldsymbol{v}' \otimes \boldsymbol{v}')_{\tilde{\Omega}^f_t} + (\boldsymbol{v}' \cdot \nabla_x \boldsymbol{w}^f \overline{\tau}, \boldsymbol{v}' \cdot \nabla_x \boldsymbol{v})_{\tilde{\Omega}^f_t}$$

$$\tag{51}$$

and

$$F^f_{MS}(\{\boldsymbol{w}^f, q^f\}) = F^f(\{\boldsymbol{w}^f, q^f\}). \tag{52}$$

The following definitions of terms are employed in (51):

$$\boldsymbol{v}' = \tau_M(\mathcal{L}^f(\boldsymbol{v}, p; \hat{\boldsymbol{v}}) - \rho^f \boldsymbol{f}^f) \tag{53}$$

$$\tau_M = (\frac{C_t}{\Delta t^2} + (\boldsymbol{v} - \hat{\boldsymbol{v}}) \cdot \boldsymbol{G}(\boldsymbol{v} - \hat{\boldsymbol{v}}) + C_I(\frac{\mu^f}{\rho^f})^2 \boldsymbol{G} : \boldsymbol{G})^{-1/2} \tag{54}$$

$$\tau_C = (\tau_M \boldsymbol{g} \cdot \boldsymbol{g})^{-1} \tag{55}$$

$$\overline{\tau} = (\boldsymbol{v}' \cdot \boldsymbol{G} \boldsymbol{v}')^{-1/2} \tag{56}$$

$$G_{ij} = \sum_{k=1}^{d} \frac{\partial \xi_k}{\partial x_i} \frac{\partial \xi_k}{\partial x_j} \tag{57}$$

$$\boldsymbol{G} : \boldsymbol{G} = \sum_{i,j=1}^{d} G_{ij} G_{ij} \tag{58}$$

$$(\boldsymbol{v} - \hat{\boldsymbol{v}}) \cdot \boldsymbol{G}(\boldsymbol{v} - \hat{\boldsymbol{v}}) = \sum_{i,j=1}^{d} (v_i - \hat{v}_i) G_{ij} (v_j - \hat{v}_j) \tag{59}$$

$$g_i = \sum_{j=1}^{d} \frac{\partial \xi_j}{\partial x_i}, \tag{60}$$

$$\boldsymbol{g} \cdot \boldsymbol{g} = g_i g_i. \tag{61}$$

13

In the above, $\frac{\partial \boldsymbol{\xi}}{\partial \boldsymbol{x}}$ is the inverse Jacobian of the mapping between the isoparametric, or parent, and physical domains, Δt is the time step, and C_I is a positive constant, independent of the mesh size, derived from an element-wise inverse estimate (see, e.g., Johnson [25]). In (50) the symbol $\tilde{\Omega}_t^f$ is used to denote the fact that integrals are taken over element interiors.

Galerkin's method is employed for the solid and mesh motion problems. The fluid formulation (51) emanates from the variational multiscale residual-based turbulence modeling paradigm [1, 4, 6]. Residual-based formulation of fluid flow may be viewed as an extension of well-known stabilized methods, such as SUPG [7]. However, the last term of (51) is not motivated by multiscale arguments, but merely provides additional residual-based stabilization (see Taylor, Hughes, and Zarins [45]).

Remark 3.1 *Our coupled semi-discrete formulation (50) satisfies global conservation of mass and linear momentum (see [2]). Note that the convective term in (50) is written in the advective form. The advantage of the advective form is that it trivially satisfies the so-called Discrete Geometric Conservation Law (DGCL). The DGCL states that for solenoidal material particle velocity fields, in the absence of body forces and surface tractions, the discrete scheme must preserve the state of constant solution. Discussion of the importance of conservation and satisfaction of the DGCL for moving domain problems is given in [11, 13, 28]*

3.3   Time integration of the FSI system

In this section we present the time integration scheme for the semi-discrete equations (50), namely, the generalized-α method (see [2, 8, 24]). The algorithm presented here is essentially the same procedure as proposed in [2], with a modification introduced at the level of the nonlinear iteration. The modification consists of removing the so-called shape derivatives from the left-hand-side tangent matrix, thus decoupling the mesh motion solve from the rest of the nonlinear system.

Let $\boldsymbol{U}$, $\dot{\boldsymbol{U}}$, $\ddot{\boldsymbol{U}}$, and $\boldsymbol{P}$ denote the vectors of nodal or control variable degrees of freedom of displacement, velocity, acceleration and pressure, respectively, of the fluid-structure system [1]. Let $\boldsymbol{V}$, $\dot{\boldsymbol{V}}$, and $\ddot{\boldsymbol{V}}$ denote the vectors of nodal or control variable degrees of freedom of mesh displacement, velocity, and acceleration, respectively. We first define three residual vectors corresponding to the momentum, continuity, and mesh motion equations by substituting individual basis functions in

---

[1]   This interpretation is strict in the solid, and in the fluid $\dot{\boldsymbol{U}}$ represents the particle velocity, but $\ddot{\boldsymbol{U}}$ represents its derivative holding the mesh point fixed and so it is not actually the particle acceleration. Furthermore, in the fluid, $\boldsymbol{U}$ plays no role whatsoever.

place of $\boldsymbol{w}^f$, $\boldsymbol{w}^s$, q^f, and $\boldsymbol{w}^m$ in (50) as follows:

$$\boldsymbol{R}^{mom} = [R^{mom}_{A,i}] \tag{62}$$

$$R^{mom}_{A,i} = B^f_{MS}(\{N_A\boldsymbol{e}_i, 0\}, \{\boldsymbol{v}, p\}; \hat{\boldsymbol{v}}) - F^f_{MS}(\{N_A\boldsymbol{e}_i, 0\})$$
$$+ B^s(\hat{N}_A\boldsymbol{e}_i, \boldsymbol{u}) - F^s(\hat{N}_A\boldsymbol{e}_i) \tag{63}$$

$$\boldsymbol{R}^{cont} = [R^{cont}_A] \tag{64}$$

$$R^{cont}_A = B^f_{MS}(\{\boldsymbol{0}, N_A\}, \{\boldsymbol{v}, p\}; \hat{\boldsymbol{v}}) - F^f_{MS}(\{\boldsymbol{0}, N_A\}) \tag{65}$$

$$\boldsymbol{R}^{mesh} = [R^{mesh}_{A,i}] \tag{66}$$

$$R^{mesh}_{A,i} = B^m(\tilde{N}_A\boldsymbol{e}_i, \hat{\boldsymbol{u}}), \tag{67}$$

where $\boldsymbol{e}_i$ is the ith Cartesian basis vector.

We now state the equations of the generalized-α time integration method: given $(\boldsymbol{U}_n, \dot{\boldsymbol{U}}_n, \ddot{\boldsymbol{U}}_n, \boldsymbol{V}_n, \dot{\boldsymbol{V}}_n, \ddot{\boldsymbol{V}}_n)$, the solution at the previous time step, find $(\boldsymbol{U}_{n+1}, \dot{\boldsymbol{U}}_{n+1}, \ddot{\boldsymbol{U}}_{n+1}, \boldsymbol{P}_{n+1}, \boldsymbol{V}_{n+1}, \dot{\boldsymbol{V}}_{n+1}, \ddot{\boldsymbol{V}}_{n+1}, \boldsymbol{U}_{n+\alpha_f}, \dot{\boldsymbol{U}}_{n+\alpha_f}, \ddot{\boldsymbol{U}}_{n+\alpha_m}, \boldsymbol{V}_{n+\alpha_f}, \dot{\boldsymbol{V}}_{n+\alpha_f}, \ddot{\boldsymbol{V}}_{n+\alpha_m})$, the solution at the current and intermediate time steps, such that

$$\boldsymbol{R}^{mom}(\boldsymbol{U}_{n+\alpha_f}, \dot{\boldsymbol{U}}_{n+\alpha_f}, \ddot{\boldsymbol{U}}_{n+\alpha_m}, \boldsymbol{P}_{n+1}, \boldsymbol{V}_{n+\alpha_f}, \dot{\boldsymbol{V}}_{n+\alpha_f}, \ddot{\boldsymbol{V}}_{n+\alpha_m}) = \boldsymbol{0}, \tag{68}$$

$$\boldsymbol{R}^{cont}(\boldsymbol{U}_{n+\alpha_f}, \dot{\boldsymbol{U}}_{n+\alpha_f}, \ddot{\boldsymbol{U}}_{n+\alpha_m}, \boldsymbol{P}_{n+1}, \boldsymbol{V}_{n+\alpha_f}, \dot{\boldsymbol{V}}_{n+\alpha_f}, \ddot{\boldsymbol{V}}_{n+\alpha_m}) = \boldsymbol{0}, \tag{69}$$

$$\boldsymbol{R}^{mesh}(\boldsymbol{U}_{n+\alpha_f}, \dot{\boldsymbol{U}}_{n+\alpha_f}, \ddot{\boldsymbol{U}}_{n+\alpha_m}, \boldsymbol{P}_{n+1}, \boldsymbol{V}_{n+\alpha_f}, \dot{\boldsymbol{V}}_{n+\alpha_f}, \ddot{\boldsymbol{V}}_{n+\alpha_m}) = \boldsymbol{0}, \tag{70}$$

$$\boldsymbol{U}_{n+\alpha_f} = \boldsymbol{U}_n + \alpha_f(\boldsymbol{U}_{n+1} - \boldsymbol{U}_n), \tag{71}$$

$$\dot{\boldsymbol{U}}_{n+\alpha_f} = \dot{\boldsymbol{U}}_n + \alpha_f(\dot{\boldsymbol{U}}_{n+1} - \dot{\boldsymbol{U}}_n), \tag{72}$$

$$\ddot{\boldsymbol{U}}_{n+\alpha_m} = \ddot{\boldsymbol{U}}_n + \alpha_m(\ddot{\boldsymbol{U}}_{n+1} - \ddot{\boldsymbol{U}}_n), \tag{73}$$

$$\boldsymbol{V}_{n+\alpha_f} = \boldsymbol{V}_n + \alpha_f(\boldsymbol{V}_{n+1} - \boldsymbol{V}_n), \tag{74}$$

$$\dot{\boldsymbol{V}}_{n+\alpha_f} = \dot{\boldsymbol{V}}_n + \alpha_f(\dot{\boldsymbol{V}}_{n+1} - \dot{\boldsymbol{V}}_n), \tag{75}$$

$$\ddot{\boldsymbol{V}}_{n+\alpha_m} = \ddot{\boldsymbol{V}}_n + \alpha_m(\ddot{\boldsymbol{V}}_{n+1} - \ddot{\boldsymbol{V}}_n), \tag{76}$$

$$\dot{\boldsymbol{U}}_{n+1} = \dot{\boldsymbol{U}}_n + \Delta t((1 - \gamma)\ddot{\boldsymbol{U}}_n + \gamma\ddot{\boldsymbol{U}}_{n+1}), \tag{77}$$

$$\boldsymbol{U}_{n+1} = \boldsymbol{U}_n + \Delta t\dot{\boldsymbol{U}}_n + \frac{\Delta t^2}{2}((1 - 2\beta)\ddot{\boldsymbol{U}}_n + 2\beta\ddot{\boldsymbol{U}}_{n+1}), \tag{78}$$

$$\dot{\boldsymbol{V}}_{n+1} = \dot{\boldsymbol{V}}_n + \Delta t((1 - \gamma)\ddot{\boldsymbol{V}}_n + \gamma\ddot{\boldsymbol{V}}_{n+1}), \tag{79}$$

$$\boldsymbol{V}_{n+1} = \boldsymbol{V}_n + \Delta t\dot{\boldsymbol{V}}_n + \frac{\Delta t^2}{2}((1 - 2\beta)\ddot{\boldsymbol{V}}_n + 2\beta\ddot{\boldsymbol{V}}_{n+1}), \tag{80}$$

where $\Delta t = t_{n+1} - t_n$ is the time step, α_f, α_m, γ, and β are real-valued parameters that define the method and are selected to ensure second-order accuracy and unconditional stability (see [2] for details).

To solve the nonlinear system of equations (68)-(80), we employ the following modified version of the predictor-multicorrector algorithm presented in [2]:

Predictor stage. Set

$$\dot{U}_{n+1,(0)} = \dot{U}_n, \tag{81}$$

$$\ddot{U}_{n+1,(0)} = \frac{(\gamma - 1)}{\gamma}\ddot{U}_n, \tag{82}$$

$$U_{n+1,(0)} = U_n + \Delta t\dot{U}_n + \frac{\Delta t^2}{2}((1 - 2\beta)\ddot{U}_n + 2\beta\ddot{U}_{n+1,(0)}), \tag{83}$$

$$P_{n+1,(0)} = P_n, \tag{84}$$

$$\dot{V}_{n+1,(0)} = \dot{V}_n \tag{85}$$

$$\ddot{V}_{n+1,(0)} = \frac{(\gamma - 1)}{\gamma}\ddot{V}_n \tag{86}$$

$$V_{n+1,(0)} = V_n + \Delta t\dot{V}_n + \frac{\Delta t^2}{2}((1 - 2\beta)\ddot{V}_n + 2\beta\ddot{V}_{n+1,(0)}), \tag{87}$$

where the subscript 0 on the left-hand-side quantities is the iteration index.

Multi-corrector stage. Repeat the following steps for $l = 1, 2, \ldots, l_{max}$.

(1) Evaluate iterates at the intermediate time levels as

$$U_{n+\alpha_f,(l)} = U_n + \alpha_f(U_{n+1,(l-1)} - U_n) \tag{88}$$

$$\dot{U}_{n+\alpha_f,(l)} = \dot{U}_n + \alpha_f(\dot{U}_{n+1,(l-1)} - \dot{U}_n) \tag{89}$$

$$\ddot{U}_{n+\alpha_m,(l)} = \ddot{U}_n + \alpha_m(\ddot{U}_{n+1,(l-1)} - \ddot{U}_n) \tag{90}$$

$$V_{n+\alpha_f,(l)} = V_n + \alpha_f(V_{n+1,(l-1)} - V_n) \tag{91}$$

$$\dot{V}_{n+\alpha_f,(l)} = \dot{V}_n + \alpha_f(\dot{V}_{n+1,(l-1)} - \dot{V}_n) \tag{92}$$

$$\ddot{V}_{n+\alpha_m,(l)} = \ddot{V}_n + \alpha_m(\ddot{V}_{n+1,(l-1)} - \ddot{V}_n) \tag{93}$$

$$P_{n+1,(l)} = P_{n+1,(l-1)} \tag{94}$$

(2) Use the intermediate solutions to assemble the residuals of the continuity and momentum equations, and the corresponding matrices in the linear system

$$\frac{\partial R^{mom}}{\partial \ddot{U}_{n+1}}\Delta\ddot{U}_{n+1,(l)} + \frac{\partial R^{mom}}{\partial P_{n+1}}\Delta P_{n+1,(l)} = -R^{mom}_{(l)} \tag{95}$$

$$\frac{\partial R^{con}}{\partial \ddot{U}_{n+1}}\Delta\ddot{U}_{n+1,(l)} + \frac{\partial R^{con}}{\partial P_{n+1}}\Delta P_{n+1,(l)} = -R^{con}_{(l)} \tag{96}$$

Solve this linear system using a preconditioned GMRES algorithm (see Saad and Shultz [39]) to a specified tolerance.

(3) Having solved the linear system, update the iterates as

$$\ddot{U}_{n+1,(l)} = \ddot{U}_{n+1,(l-1)} + \Delta\ddot{U}_{n+1,(l)} \tag{97}$$

$$\dot{U}_{n+1,(l)} = \dot{U}_{n+1,(l-1)} + \gamma\Delta t\Delta\ddot{U}_{n+1,(l)} \tag{98}$$

$$U_{n+1,(l)} = U_{n+1,(l-1)} + \beta(\Delta t)^2\Delta\ddot{U}_{n+1,(l)} \tag{99}$$

$$P_{n+1,(l)} = P_{n+1,(l-1)} + \Delta P_{n+1,(l)} \tag{100}$$

(4) Equate the solid and mesh displacement, velocity, and acceleration degrees of freedom for the fluid-solid interface, and evaluate mesh motion variables at the intermediate time level as

$$\boldsymbol{V}_{A,n+1,(l-1)} = \boldsymbol{U}_{A,n+1,(l)} \ \forall A \ I_{fs} \tag{101}$$

$$\dot{\boldsymbol{V}}_{A,n+1,(l-1)} = \dot{\boldsymbol{U}}_{A,n+1,(l)} \ \forall A \ I_{fs} \tag{102}$$

$$\ddot{\boldsymbol{V}}_{A,n+1,(l-1)} = \ddot{\boldsymbol{U}}_{A,n+1,(l)} \ \forall A \ I_{fs} \tag{103}$$

$$\boldsymbol{V}_{n+\alpha_f,(l)} = \boldsymbol{V}_n + \alpha_f(\boldsymbol{V}_{n+1,(l-1)} - \boldsymbol{V}_n) \tag{104}$$

$$\dot{\boldsymbol{V}}_{n+\alpha_f,(l)} = \dot{\boldsymbol{V}}_n + \alpha_f(\dot{\boldsymbol{V}}_{n+1,(l-1)} - \dot{\boldsymbol{V}}_n) \tag{105}$$

$$\ddot{\boldsymbol{V}}_{n+\alpha_m,(l)} = \ddot{\boldsymbol{V}}_n + \alpha_m(\ddot{\boldsymbol{V}}_{n+1,(l-1)} - \ddot{\boldsymbol{V}}_n) \tag{106}$$

$$\tag{107}$$

(5) Use the intermediate solutions to assemble the residuals of the mesh motion equations and the corresponding matrix in the linear system

$$\frac{\partial \boldsymbol{R}^{mesh}}{\partial \ddot{\boldsymbol{V}}_{n+1}} \Delta \ddot{\boldsymbol{V}}_{n+1,(l)} = -\boldsymbol{R}^{mesh}_{(l)} \tag{108}$$

$$\tag{109}$$

Solve this linear system using a preconditioned Conjugate Gradient algorithm (see, e.g., [16]) to a specified tolerance.

(6) Having solved the linear system, update the mesh motion iterates as

$$\ddot{\boldsymbol{V}}_{n+1,(l)} = \ddot{\boldsymbol{V}}_{n+1,(l-1)} + \Delta \ddot{\boldsymbol{V}}_{n+1,(l)} \tag{110}$$

$$\dot{\boldsymbol{V}}_{n+1,(l)} = \dot{\boldsymbol{V}}_{n+1,(l-1)} + \gamma \Delta t \Delta \ddot{\boldsymbol{V}}_{n+1,(l)} \tag{111}$$

$$\boldsymbol{V}_{n+1,(l)} = \boldsymbol{V}_{n+1,(l-1)} + \beta (\Delta t)^2 \Delta \ddot{\boldsymbol{V}}_{n+1,(l)} \tag{112}$$

Remark 3.2 *As mentioned earlier in this section, the above modification to the originally proposed method consists of omitting the influence of the mesh motion variables on the residuals of the fluid mechanics equations in the left-hand-side matrix. This modification leads to two uncoupled linear solves: one for the coupled fluid-solid system and another for the mesh motion. It is beneficial from the standpoint of linear equation solving, since one needs to solve two smaller linear systems rather than one large one.*

Remark 3.3 *Although this strategy leads to an inconsistent tangent matrix for the coupled nonlinear equation system, we did not observe significant decrease in nonlinear convergence. In fact, we recommend using this strategy for blood flow computations.*

Remark 3.4 *Tezduyar et al. [48, 49, 51] refer to this strategy as "quasi-direct" coupling and advocate its use in many applications, including arterial flows.*

17

4 Flow in a patient-specific thoracic aorta with an implanted left ventricular assist device

(a) Patient-specific model of
the thoracic aorta

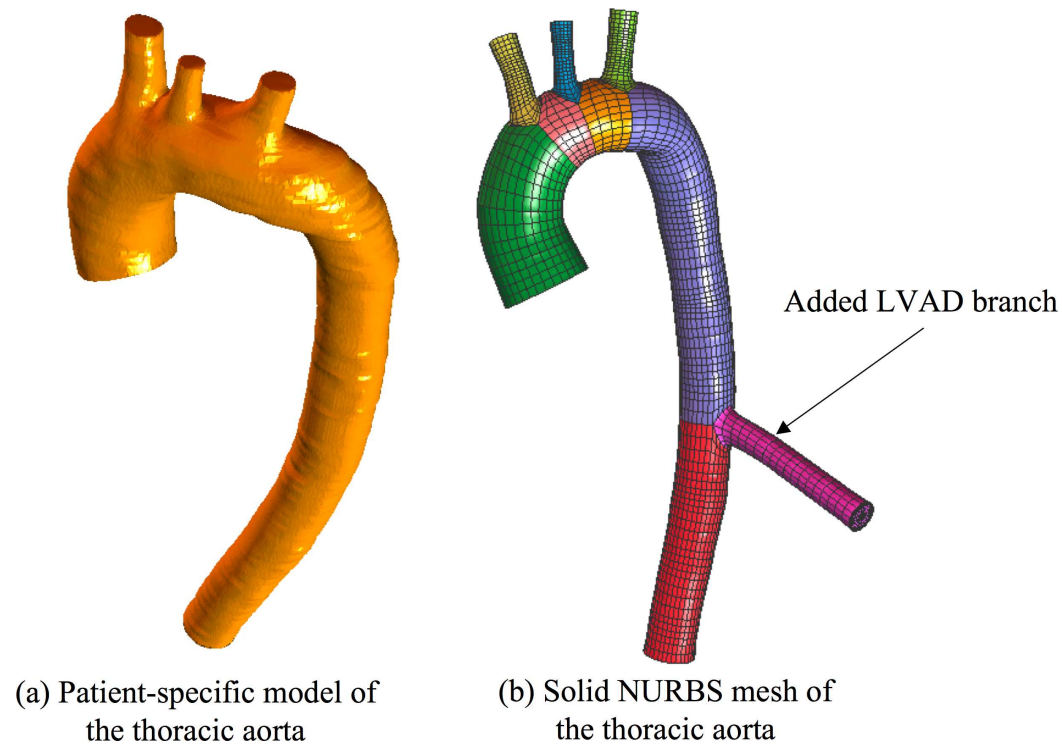(b) Solid NURBS mesh of
the thoracic aorta

Fig. 2. Flow in a patient-specific thoracic aorta with LVAD. (a) Patient-specific model constructed from imaging data; (c) Smoothed solid NURBS model and mesh with the LVAD branch added. For more details of geometrical modeling for isogeometric analysis of blood flow the reader is referred to [54].

Patient-specific geometry of the thoracic aorta of an over-30-year-old healthy volunteer was obtained from 64-slice CT angiography. The geometrical model is shown in Figure 2(a) . The computational mesh, consisting of 44892 quadratic NURBS elements, is shown in Figure 2(b), where an additional branch was added to the model to represent the inflow from the left ventricular assist device. Wall thickness for this model is taken to be 15% of the nominal radius of each cross-section of the fluid domain model. Two quadratic NURBS elements and four C^1-continuous basis functions are used for through-thickness resolution of the arterial wall.

We employ the following material properties in our computations. The fluid density and dynamic viscosity are $\rho^f = 1.06 \text{g/cm}^3$ and $\mu^f = 0.04$ g/cm s, respectively. The solid has the density $\rho^s = 1$ g/cm^3, Young's modulus, $E = 4.144 \times 10^6$ dyn/cm^2, and Poisson's ratio, $\nu = 0.45$. The density and Young's modulus material data are taken from [2]. The solid model coefficients μ^s and κ^s are obtained using standard relationships for the Lamé constants (see, e.g., Gould [17]).

$$\sigma_n = C_3 q + p_0$$

$$\sigma_n = C_2 q + p_0$$

$$\sigma_n = C_4 q + p_0$$

Inflow with
period T (s)

Inflow with
period T (s)

$$\sigma_n = C_1 q + p_0$$
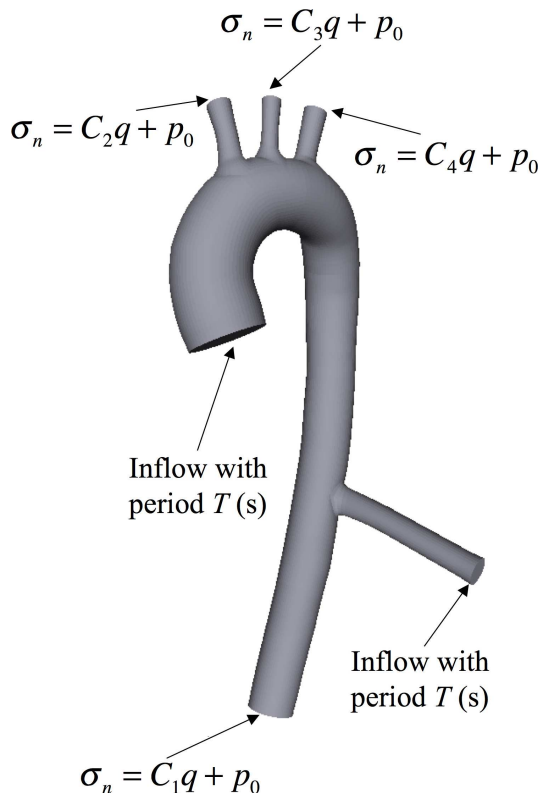
Fig. 3. Flow in a patient-specific thoracic aorta with LVAD. Boundary conditions for the fluid domain. $C_a, a = 1, 2, 3, 4$, are the resistance constants, σ_n is the normal component of the traction vector, q is the volumetric flowrate, and p_0 is responsible for setting the physiological pressure level in the blood vessels.

We fix the solid at the inlet and at all outlets. The top 50% of the right and left innominate and subclavian arteries are also constrained not to move. This is done so as to avoid the non-physical swinging motion of the thoracic aorta during the simulation. Constraining these portions of these arteries mimics the effect of the surrounding tissue in a very crude way. Further research in accounting for the surrounding tissue is necessary, with respect to both mathematical modeling and computation. The LVAD branch is also assumed rigid.

Our model has two inflow boundaries, the inlet of the ascending aorta and the inlet of the LVAD branch, where we specify a periodic flow waveform. These inflow waveforms are provided by the lumped-parameter model of the cardiovascular system that also includes ventricular assist. Our model also has various outlets where resistance boundary conditions are applied. A brief description of the lumped-parameter model and its output for patient-specific simulations performed in this paper, as well as imposition of resistance boundary conditions, is given in the following sections. See Figure 3 for a sketch of the placement of boundary conditions.

4.1.1 *Lumped-parameter model of the cardiovascular system and inflow boundary conditions*

A lumped-parameter closed-loop multiscale model of the cardiovascular system has been developed in [15] based on the framework of Olufsen [38]. Both the systemic and pulmonary circulation have been modeled to close the loop around the area of focus, the aorta and large arteries. Several modeling techniques have been employed to complete the loop. A varying elastance representation has been used to describe the beating heart. A dynamic aortic valve model has been developed to capture valve motion which allows for regurgitant flow during closure at the onset of diastole. Pressure and flow along the length of the systemic large arteries are determined using the quasi-one-dimensional Navier-Stokes equations for Newtonian flow in an elastic tube coupled with a pressure/area state equation (see, e.g., Hughes [21], Hughes and Lubliner [23], Lighthill [31], Olufsen [37]). The small arteries are represented with a complex impedance based on their diameter and elastic properties [36]. The systemic venous return and pulmonary circulation have been represented using lumped parameter models. The coronary arteries are modeled using a lumped parameter model with varying resistances and intramyocardial pressure fluctuations.

The lumped-parameter cardiovascular model allows for the inclusion of the left ventricular assist device. In this particular case, we are studying the Jarvik 2000 model, which is a continuous-flow rotary blood pump. Because of the rotary nature of Jarvik 2000, commonly employed pressure-flow curves can be used to describe resultant flow rates over a range of pressures and pump speeds. The pump is introduced into the model as the additional outflow from the left ventricle and the additional inflow to the arterial tree. In this work, we consider three pump settings: 1) pump is off; 2) pump is operating at the angular speed of 8,000 rpm; 3) pump is operating at the angular speed of 10,000 rpm. Periodic flowrates through the aorta and the LVAD inlets, with period $T = 0.6667$ s, are computed using the lumped-parameter cardiovascular model, and the results are illustrated in Figure 4. In the case when the pump is off, all the flow comes through the inflow of the aorta. In the case of 8,000 rpm, the LVAD supplies more than 50% of the flow. Finally, in the case of 10,000 rpm, almost all of the flow comes from the LVAD. It is the latter case that is of most concern with respect to complications arizing from flow stasis. We note that the case when the pump is off corresponds to the so-called "weak heart" condition, because the volume of blood supplied by the heart during a heart cycle is somewhat smaller that it would be in the heathy case.

We use the model outputs for the three pump settings as boundary conditions for our patient-specific model, which results in a simple, one-way coupled simulation. A more faithful representation of reality would consist of embedding our patient-specific model inside the lumped-parameter cardiovascular model discussed here with a full two-way coupling. We hope to pursue this in the future.
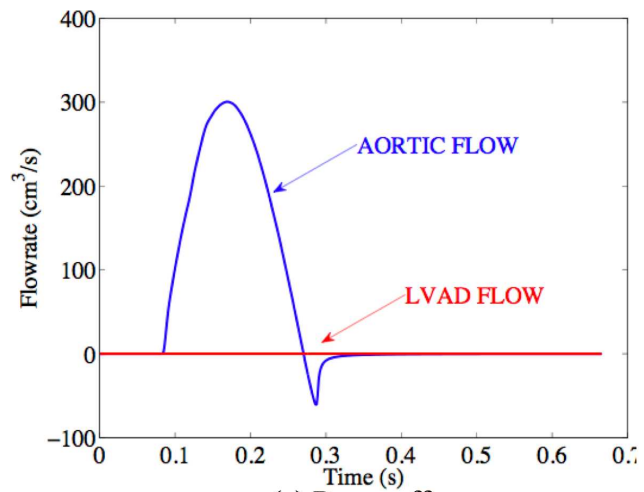
(a) Pump off
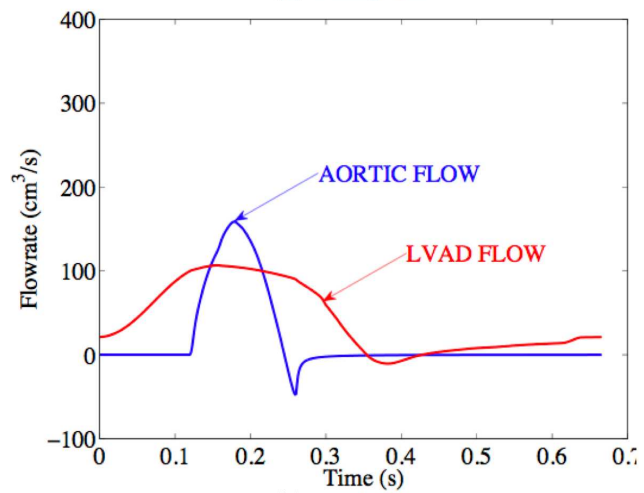
(b) 8,000 rpm
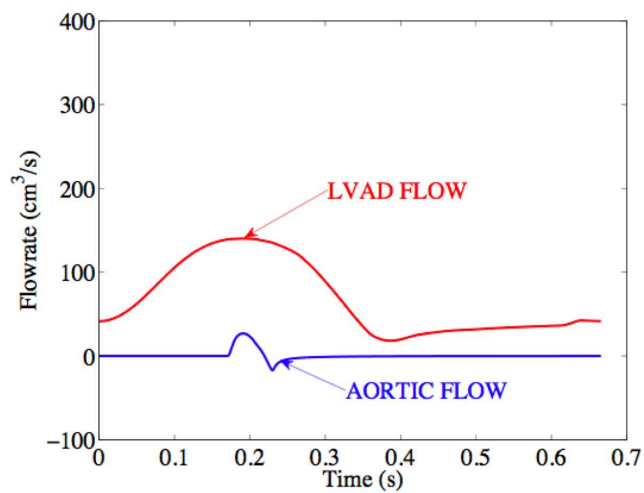
(c) 10,000 rpm

Fig. 4. Inflow flowrate curves obtained by computing

4.1.2 Outflow boundary conditions

In order to ensure physiologically-realistic response, resistance boundary conditions must be applied in such a way that physiological pressure levels are present in the system at all times. This is accomplished by making use of the following variant of the resistance boundary condition (see also Figueroa *et al.* [12], Vignon-Clementel *et al.* [52], and Heywood *et al.* [19]). We assume that all outlet faces, denoted by Γ_a, where a is the outflow boundary index, are fixed in space. At every outlet face Γ_a we set

$$n^T \tilde{\sigma} n + C_a \int_{\Gamma_a} v \cdot n d\Gamma_a + p_0 = 0, \tag{113}$$

$$\tau_1^T \tilde{\sigma} n = 0, \tag{114}$$

$$\tau_2^T \tilde{\sigma} n = 0 \tag{115}$$

where

$$\tilde{\sigma} n = -pn + 2\mu^f \nabla^s v \cdot n - \rho^f (\{v \cdot n\}_-)v, \tag{116}$$

the term $\{v \cdot n\}_-$ denotes the negative part of $v \cdot n$, that is

$$\begin{cases} \{v \cdot n\}_- = v \cdot n & \text{if} \quad v \cdot n < 0 \\ \{v \cdot n\}_- = 0 & \text{otherwise,} \end{cases} \tag{117}$$

n is the outward unit normal, and τ_1 and τ_2 are mutually orthogonal unit tangent vectors on the outlet face. In case of reversed flow through an outflow boundary the last term on the right-hand-side in (116) is active. Otherwise, it is identically zero and, thus, equation (113) reverts to the resistance boundary condition described in [2].

The above boundary conditions state that normal stress on the outlet face is an affine function of the flowrate through the face, while both tangential stresses are zero. The C_a's are the so-called resistance constants. They are positive, and are, in principle, different from outlet to outlet, reflecting the resistances of various blood vessels. p_0 in (113) is responsible for imposing a physiologically realistic pressure level in the vessels, even at zero flow through the outlet faces. For the computations reported in this section, p_0 is set to 85 mmHg, as in [2]. We impose boundary conditions (113) weakly by adding the following terms to the variational formulation (36)

$$\sum_a \left\{ -\int_{\Gamma_a} w^f \rho^f (\{v \cdot n\}_-)v d\Gamma_a + (\int_{\Gamma_a} w^f \cdot n d\Gamma_a) C_a (\int_{\Gamma_a} v \cdot n d\Gamma_a + p_0) \right\}, \tag{118}$$

where the sum is taken over all outlet faces with prescribed resistance conditions.

Remark 4.1 *The term,* $-\sum_a \int_{\Gamma_a} \boldsymbol{w}^f \rho^f \left(\{\boldsymbol{v} \cdot \boldsymbol{n}\}_-\right) \boldsymbol{v} d\Gamma_a$, *adds stability to the formulation in the presence of locally reversed flow through the outflow resistance boundaries. Such reverse flow occurs due to the fact that velocity fluctuations are convected out of the computational domain by the mean flow. We found that the addition of this term is important for the overall stability of the computations. In its absence we sometimes experience rapid divergence, the outlet of the descending branch of the aorta being the most vulnerable location for initiation of outflow instabilities.*

In the computations reported here, we set $C_1 = (1,500/A_1)$ dyn s/cm^5, $C_2 = (2,666/A_2)$ dyn s/cm^5, $C_3 = (1,400/A_3)$ dyn s/cm^5, $C_4 = (1,400/A_4)$ dyn s/cm^5, where $A_a, a = 1, 2, 3, 4$, are surface areas of the outlet faces (see Figure 3). This data was adapted from [38].

The constants C_a in (113) and (118) are large, and, as a result, implicit treatment of the resistance terms is beneficial for stability. The contribution of the resistance terms to the left-hand-side matrix for each outlet face Γ_a becomes

$$\alpha_f \gamma \Delta t C_a \left(\int_{\Gamma_a} N_A n_i d\Gamma_a \right) \left(\int_{\Gamma_a} N_B n_j d\Gamma_a \right), \qquad (119)$$

where the following index notation is employed: A and B are the nodal/control point indices and n_i and n_j are the Cartesian components of the unit outward normal vector to the outlet surface. Expression (119) is non-standard from the standpoint of finite element implementation in that each outlet face contributes a locally dense matrix. In our implementation, because we use iterative procedures and are interested merely in the action of (119) on a right-hand-side vector $u_{B,j}$, we do not assemble (119) directly. The action of (119) on the right-hand-side vector $u_{B,j}$ is accomplished by first multiplying $(\alpha_f \gamma \Delta t C_a)^{1/2} \left(\int_{\Gamma_a} N_B n_j d\Gamma_a \right) u_{B,j}$, which yields a scalar (summation on repeated indices B and j is assumed), and is followed by a post-multiplication by $(\alpha_f \gamma \Delta t C_a)^{1/2} \left(\int_{\Gamma_a} N_A n_i d\Gamma_a \right)$, which yields a vector that is properly dimensioned. In our software, the vector $(\alpha_f \gamma \Delta t C_a)^{1/2} \left(\int_{\Gamma_a} N_A n_i d\Gamma_a \right)$ is assembled at every outlet face Γ_a and is passed into the linear algebra routine where the multiplications take place. The procedure is perfectly parallelizable.

We initialize our computations as follows. We start with an unpressurized configuration, then we set and maintain the inflow velocity consistent with the inflow flowrate at $t = 0$, and gradually increase the pressure level in the system by raising p_0 in (113) from zero to the physiologically realistic value of 85 mmHg. This is done for a time equivalent to one or two cycles. Once the physiological pressure level is attained, we begin computing with the time-varying inflow boundary conditions until the periodic-in-time response is attained. The latter usually takes four or five cycles.

Resistance boundary condition (113) may be generalized to any other functional

23

relationship between the normal-stress and blood flow rate by replacing (113) with

$$\boldsymbol{n}^T \tilde{\boldsymbol{\sigma}} \boldsymbol{n} + f(Q_a) = 0 \tag{120}$$

where Q_a denotes the volumetric flowrate through the outlet face Γ_a, that is,

$$Q_a = \int_{\Gamma_a} \boldsymbol{v} \cdot \boldsymbol{n} d\Gamma_a, \tag{121}$$

and $f(Q_a)$ is any functional dependence, which may also include previous history, such as for impedance boundary conditions (see, e.g., [52]). In this case, (120) is imposed by adding the following terms at all the outlet faces

$$\sum_a \left\{ -\int_{\Gamma_a} \boldsymbol{w}^f \left(\{\boldsymbol{v} \cdot \boldsymbol{n}\}_- \right) \boldsymbol{v} d\Gamma_a + \left(\int_{\Gamma_a} \boldsymbol{w}^f \cdot \boldsymbol{n} d\Gamma_a \right) f(Q_a) \right\}, \tag{122}$$

and the linearization corresponding to the second term in (122) becomes

$$\alpha_f \gamma \Delta t f'(Q_a) \left(\int_{\Gamma_a} N_A n_i d\Gamma_a \right) \left(\int_{\Gamma_a} N_B n_j d\Gamma_a \right), \tag{123}$$

where $f'(Q_a)$ denotes the first derivative of f with respect to its argument evaluated at Q_a. The affine resistance of (113) is obtained by setting

$$f(Q_a) = C_a Q_a + p_0. \tag{124}$$

4.2 Numerical results

We simulate the flow-structure interaction in the patient-specific thoracic aorta with LVAD for several heart cycles. Solution data was collected for postprocessing after a nearly periodic-in-time response was attained. Figures 5-7 show the velocity magnitude on a planar cut of the model at early systole, peak systole, and late diastole. The figures clearly indicate the manner in which local blood flow features are altered due to the presence of the heart pump. Note that the magnitude of flow velocity for the cases when the pump is on is greatly increased in the vicinity of the LVAD branch. Also note the presence of very thin boundary layers associated with the pump-assisted cases. Figure 7 shows the presence of nearly turbulent structures in late diastole for the cases when the heart pump is on, while the flow structures for the unassisted simulation are unsteady, but laminar.

Figures 8-10 focus on the flow in the aortic arch. In the unassisted case, a helical flow pattern is obtained in early systole and late diastole, while in peak systole the flow vectors are aligned with the arterial path. The helical flow pattern in the aortic arch is a well-known phenomenon. For example, in [27], helical flow structures were observed in a human thoracic aorta imaged by magnetic resonance. The medium pump setting does not produce the helical flow patterns observed in the

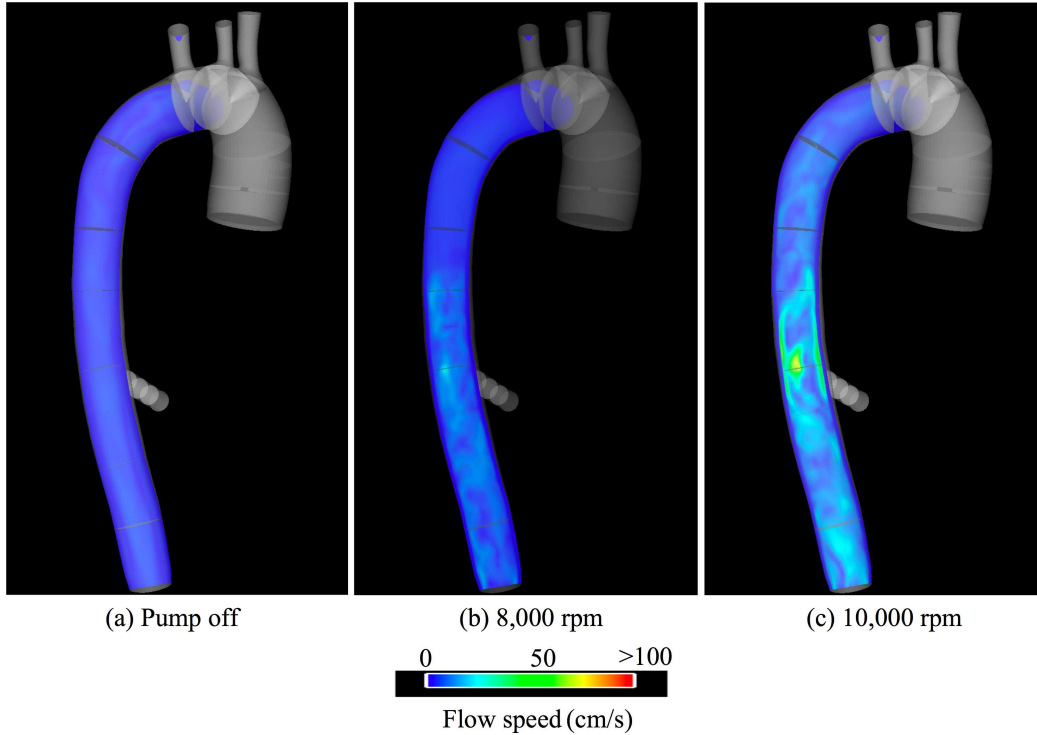|		
(a) Pump off	(b) 8,000 rpm	(c) 10,000 rpm

0   50   >100

Flow speed (cm/s)

Fig. 5. Flow in a patient-specific thoracic aorta with LVAD. Magnitude of the flow velocity on a planar longitudinal cut in early systole.

unassisted case and some flow stagnation is present in the aortic arch in early systole and late diastole. For the highest pump setting the flow in the arch is stagnant throughout the *entire* heart cycle. This is consistent with clinical observations and preliminary numerical simulations reported in [26]. Flow stagnation is known to increase uptake of atherogenic blood particles as a consequence of increased residence time, and is believed to be one of the mechanisms that is responsible for the development of atherosclerosis [14].

Figure 11 and 12 show distribution of the cycle-averaged (i.e., "mean") wall shear stress magnitude on the luminal surface. In the arch, wall shear stress is much lower for the cases when the pump is on. This observation is consistent with the predicted and observed flow stagnation in this area of the aorta. In contrast to the arch, in the descending branch near the LVAD, wall shear stress significantly exceeds healthy levels. Figures 13 and 14 focus on the arch and plot wall shear stress vectors on the luminal surface. In the unassisted case, the vectors follow the helical pattern, which is consistent with the behavior of the blood velocity in this case. For the pump-assisted simulations, the magnitude of the wall shear stress is much lower in the arch, and, furthermore, for the highest pump setting, the wall shear stress vectors point in the direction that is opposite to the conventionally assumed direction. This signifies that flow reversal occurs in the arch for the majority of the heart cycle. Figure 15 shows the so-called oscillatory shear index (OSI) distribution at the luminal surface. OSI measures the degree to which wall shear stress oscillates during

(a) Pump off   (b) 8,000 rpm   (c) 10,000 rpm
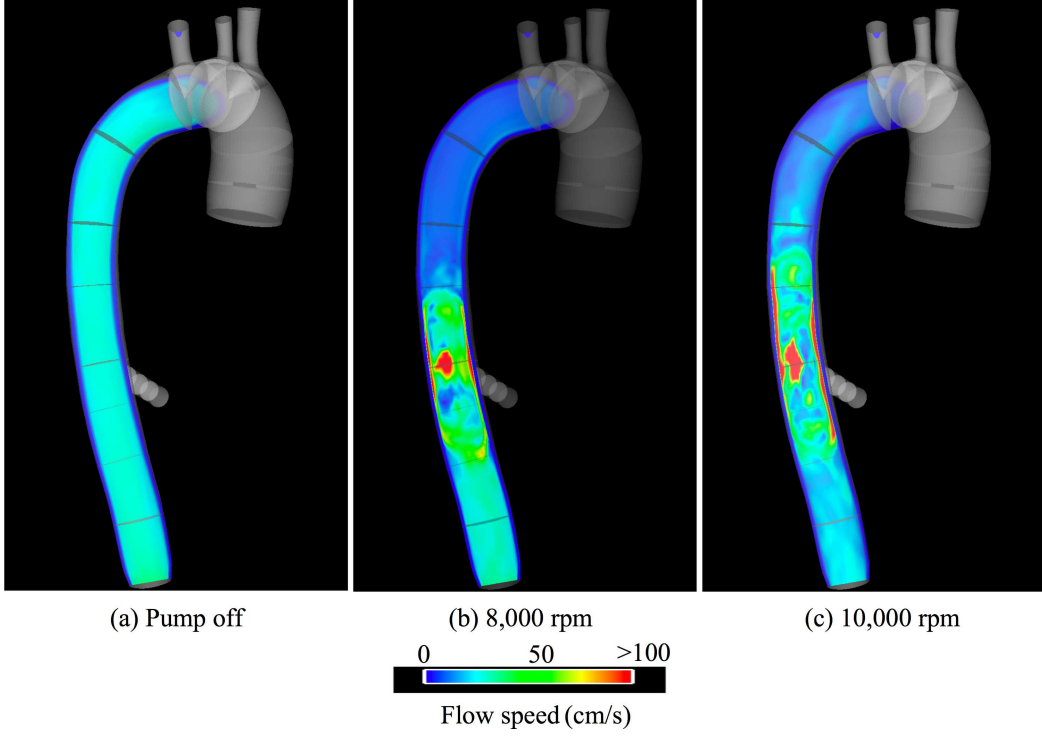
0   50   >100

Flow speed (cm/s)

Fig. 6. Flow in a patient-specific thoracic aorta with LVAD. Magnitude of the flow velocity on a planar longitudinal cut at peak systole.

the heart cycle and is defined as (see, e.g., [46, 47]):

$$\text{OSI} = \frac{1}{2}(1 - \frac{\tau_{\text{mean}}}{\tau_{\text{abs}}}), \tag{125}$$

where, denoting by $\boldsymbol{\tau}_s$ the wall shear stress vector,

$$\tau_{\text{mean}} = |\frac{1}{T}\int_0^T \boldsymbol{\tau}_s dt|, \tag{126}$$

and

$$\tau_{\text{abs}} = \frac{1}{T}\int_0^T |\boldsymbol{\tau}_s| dt. \tag{127}$$

From Figure 15(b), the OSI appears to be largest in the aortic arch for the medium pump setting. We conjecture that this occurs due to the competition between the flows coming from the inflow of the aorta and the LVAD. The relevance of wall shear stress and its temporal oscillations (as measured by OSI) to atherosclerosis is an active area of medical research (see [40] for a comprehensive review of the subject). It was shown in [29, 30] that endothelial cells subjected to elevated levels of wall shear stress tend to elongate and align in the direction of flow, and that endothelial cells that experience low or oscillatory wall shear stress remain more rounded and have no preferred alignment pattern. Moreover, exposure of the arterial wall to a relatively low wall shear stress may increase intercellular permeability and consequently increase the vulnerability of these regions of the vessel to atherosclerosis [35].
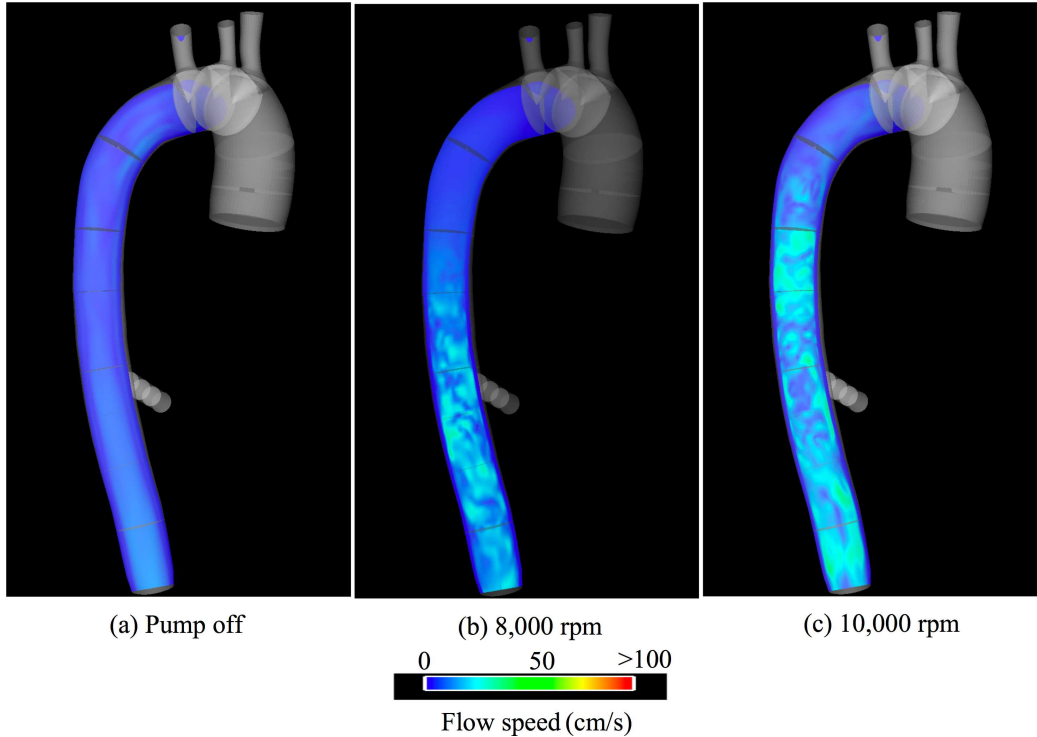
Fig. 7. Flow in a patient-specific thoracic aorta with LVAD. Magnitude of the flow velocity on a planar longitudinal cut in late diastole.

Figure 16 shows the distribution of flow among the outflow branches. It is evident that the flow distribution among the branches is very different from one pump setting to the next. This deviation of the flow distribution for the pump-assisted cases compared with the unassisted case may induce complications in the peripheral parts of the circulatory system.

5 Conclusions

Isogeometric fluid-structure interaction analysis is applied to a patient-specific model of the thoracic aorta.

A simplification to a fully-coupled solution strategy is employed in which the mesh motion is uncoupled from the rest of the system resulting in increased efficiency of the computational procedure for this type of problem. A simple modification to the outflow boundary conditions is introduced that improves stability of the numerical formulation in the presence of reversed flow.

Computational results obtained for the pump-assisted cases indicate deficiencies associated with the implantation of the LVAD in the descending branch of the thoracic aorta, specifically, abnormally high mean wall shear stress in the vicinity of the implant and abnormally low and highly oscillatory wall shear stress in the aortic

(a) Pump off   (b) 8,000 rpm   (c) 10,000 rpm

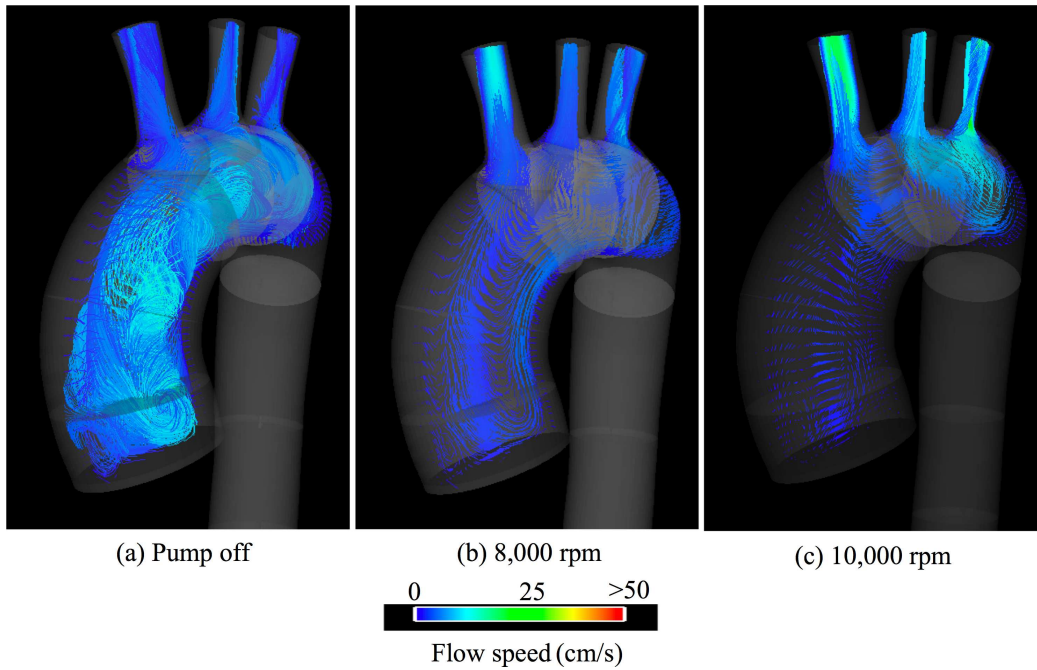0   25   >50

Flow speed (cm/s)

Fig. 8. Flow in a patient-specific thoracic aorta with LVAD. Velocity vectors colored by the velocity magnitude in the ascending aorta and the arch in early systole.
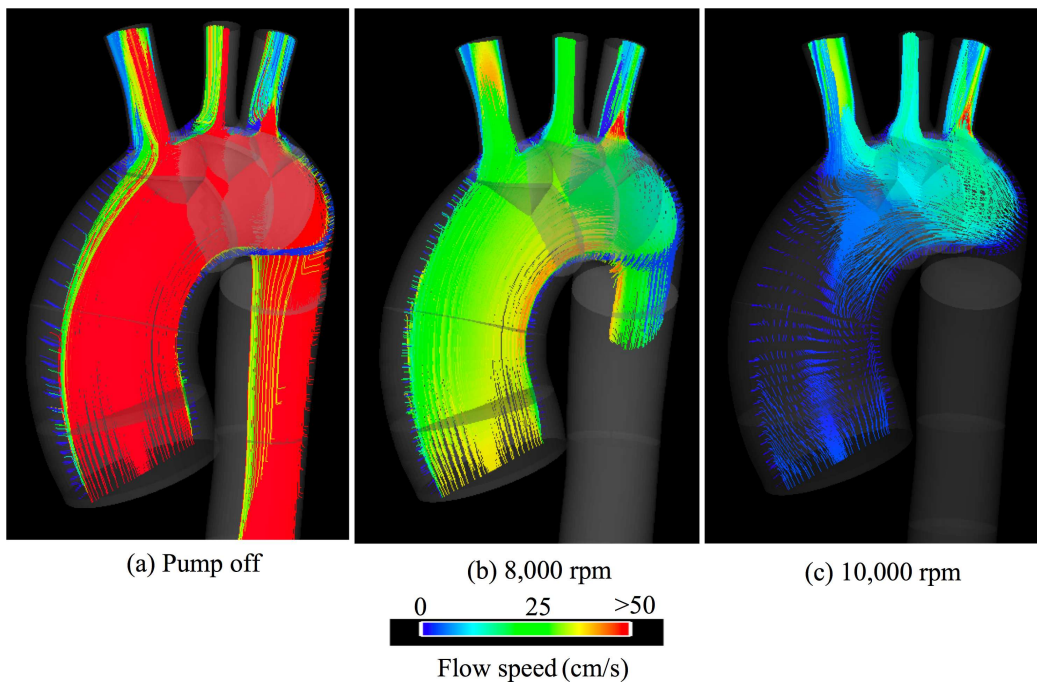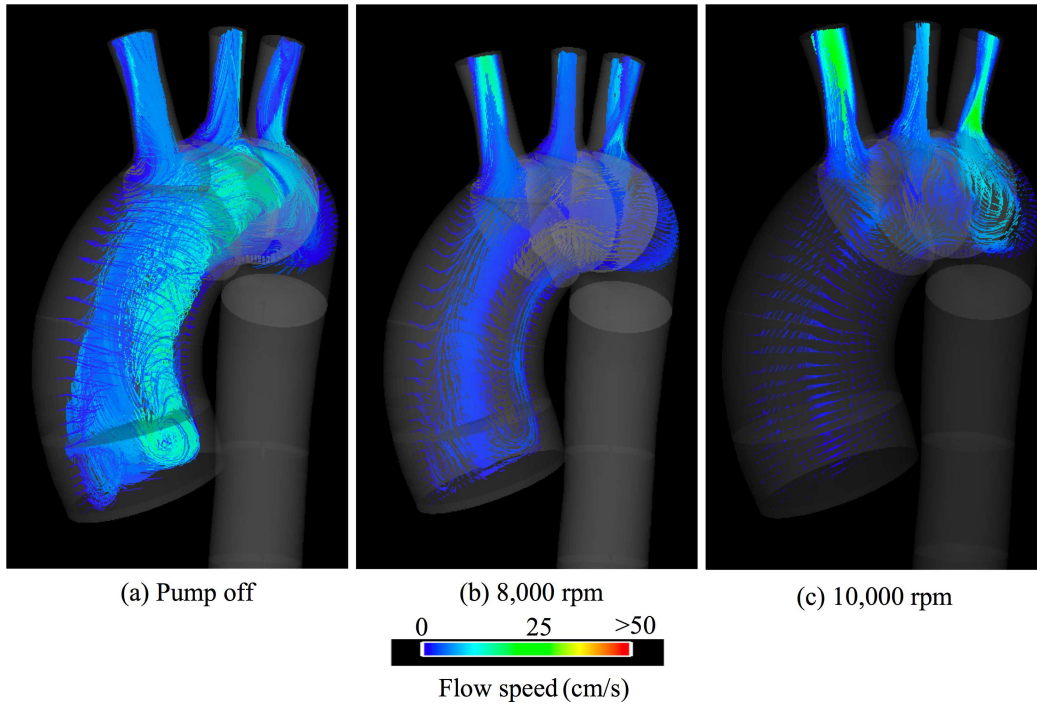

(a) Pump off   (b) 8,000 rpm   (c) 10,000 rpm

0   25   >50

Flow speed (cm/s)

Fig. 9. Flow in a patient-specific thoracic aorta with LVAD. Velocity vectors colored by the velocity magnitude in the ascending aorta and the arch at peak systole.

arch. For the highest pump speed simulation, which is most relevant in the clinical setting, blood flow stagnation in the aortic arch is observed for the entire heart cycle. Computational results are in qualitative agreement with clinical observations.

(a) Pump off   (b) 8,000 rpm   (c) 10,000 rpm

0   25   >50

Flow speed (cm/s)

Fig. 10. Flow in a patient-specific thoracic aorta with LVAD. Velocity vectors colored by the velocity magnitude in the ascending aorta and the arch in late diastole.
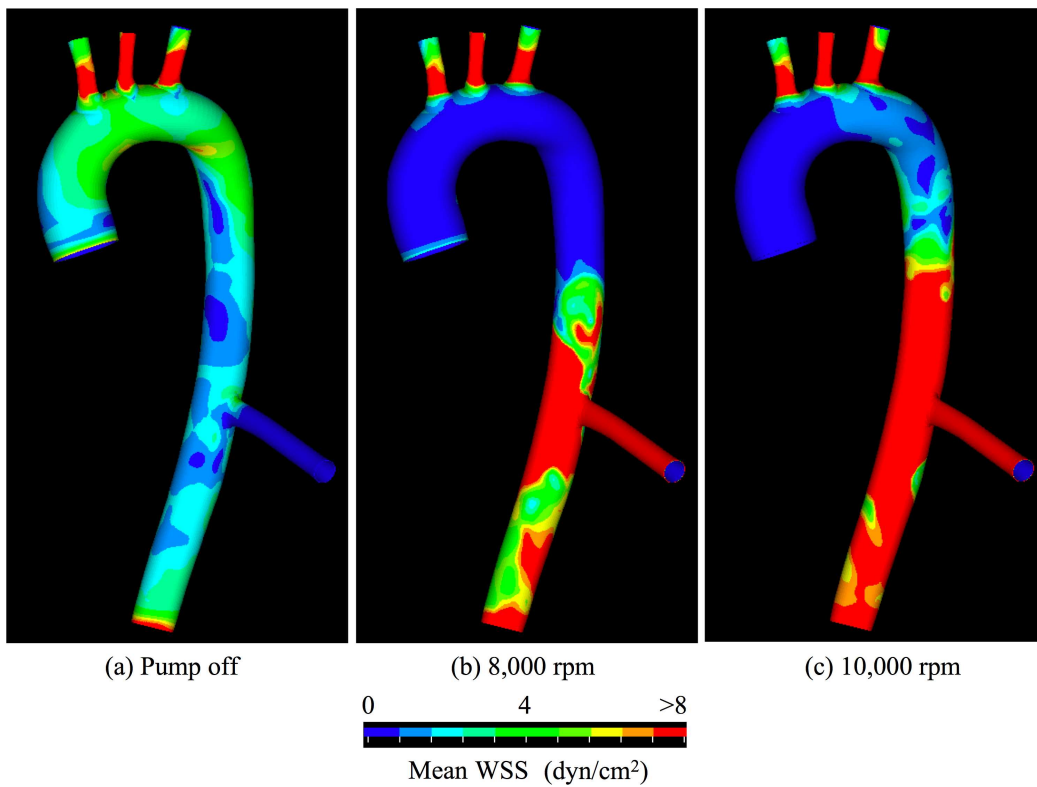

(a) Pump off   (b) 8,000 rpm   (c) 10,000 rpm

0   4   >8

Mean WSS (dyn/cm²)

Fig. 11. Flow in a patient-specific thoracic aorta with LVAD. Left lateral view of mean wall shear stress.

(a) Pump off   (b) 8,000 rpm   (c) 10,000 rpm

0   4   >8

Mean WSS (dyn/cm^2)
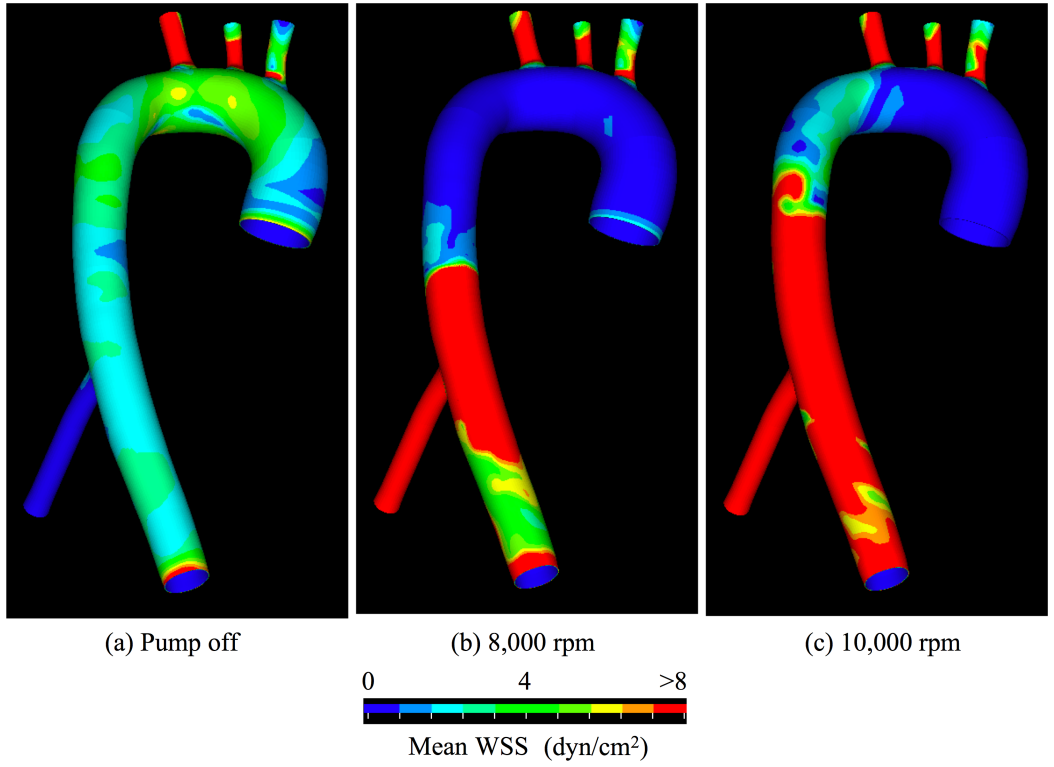
Fig. 12. Flow in a patient-specific abdominal aorta with aneurysm. Right lateral view of mean wall shear stress.
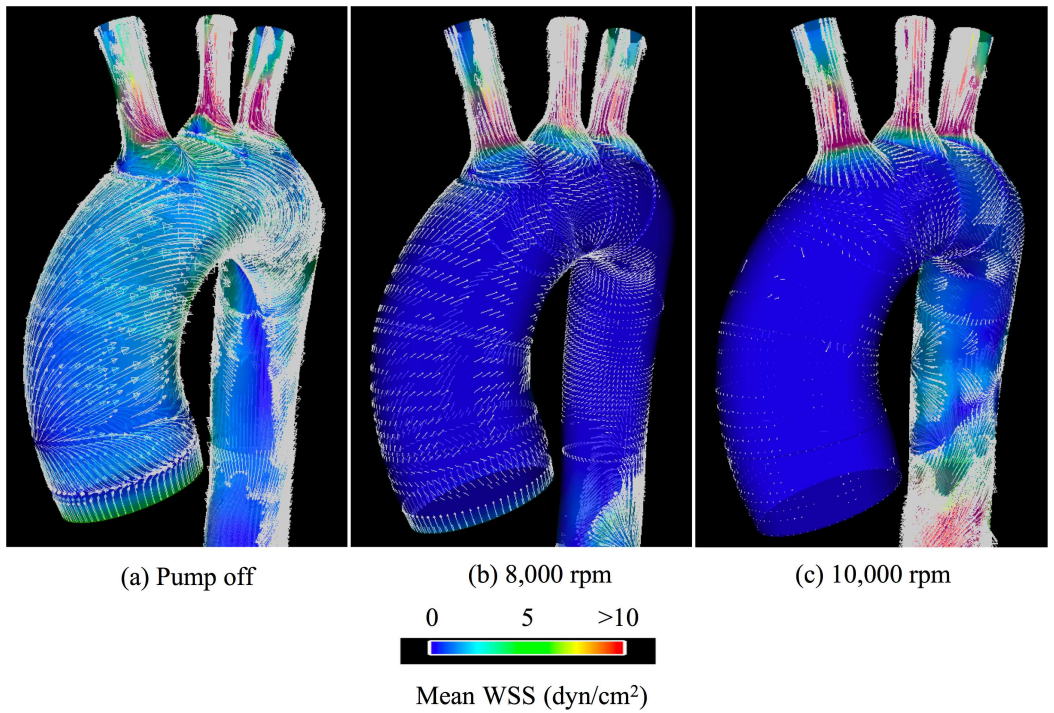
(a) Pump off   (b) 8,000 rpm   (c) 10,000 rpm

0   5   >10

Mean WSS (dyn/cm^2)

Fig. 13. Flow in a patient-specific thoracic aorta with LVAD. Mean wall shear stress vectors superposed on the magnitude of the mean wall shear stress.
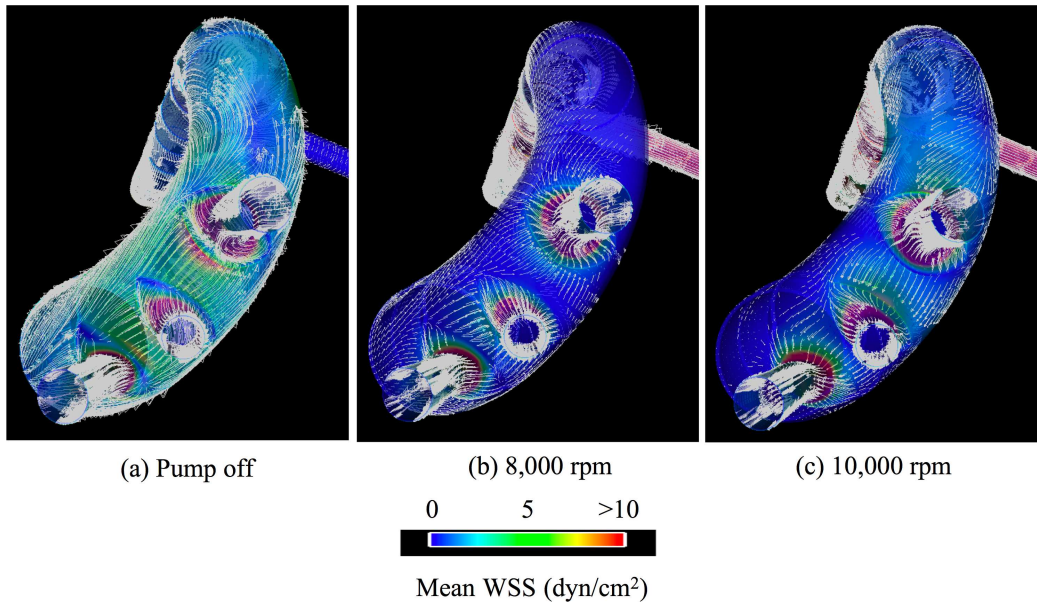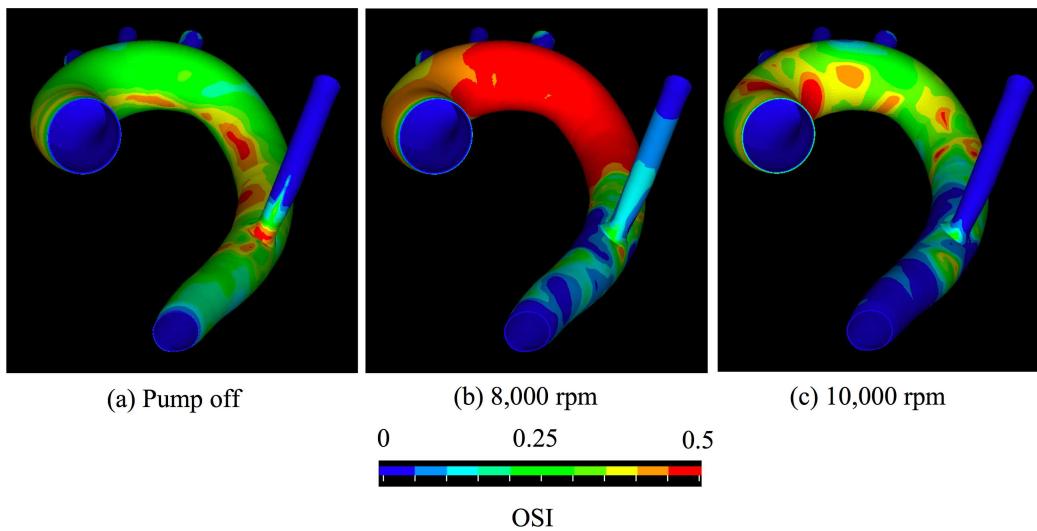
(a) Pump off   (b) 8,000 rpm   (c) 10,000 rpm

0   5   >10

Mean WSS (dyn/cm^2)

Fig. 14. Flow in a patient-specific thoracic aorta with LVAD. Mean wall shear stress vectors superposed on the magnitude of the mean wall shear stress.

(a) Pump off   (b) 8,000 rpm   (c) 10,000 rpm

0   0.25   0.5

OSI

Fig. 15. Flow in a patient-specific thoracic aorta with LVAD. Oscillatory shear index (OSI).
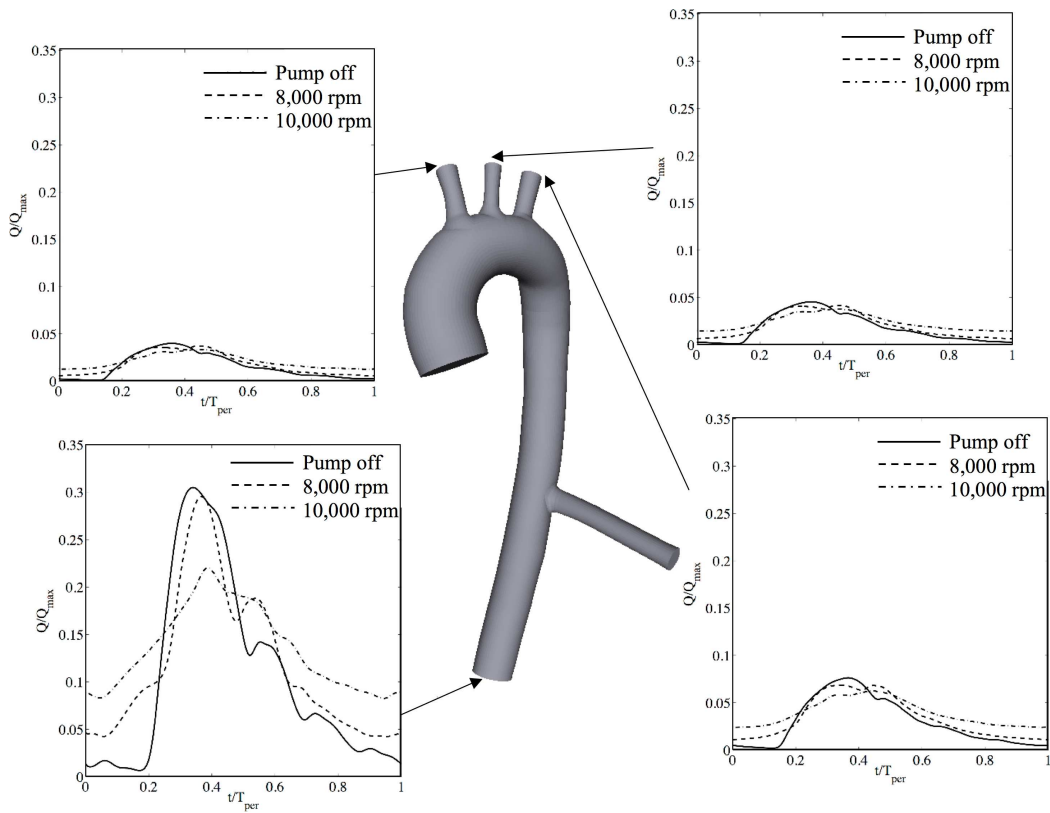
Fig. 16. Flow in a patient-specific thoracic aorta with LVAD. Flow rate distribution among outflow branches during a heart cycle. Flow rate is normalized by the maximum flow rate at peak systole for the healthy case, and time is normalized by the period of the heart cycle.

6 Acknowledgments

References

[1] I. Akkerman, Y. Bazilevs, V. M. Calo, T. J. R. Hughes, and S. Hulshoff. The role of continuity in residual-based variational multiscale modeling of turbulence. *Computational Mechanics*, 41:371–378, 2008.

[2] Y. Bazilevs, V. M. Calo, T. J. R. Hughes, and Y. Zhang. Isogeometric fluid-structure interaction: Theory, algorithms and computations. *Computational Mechanics*, 2008. Submitted.

[3] Y. Bazilevs, V. M. Calo, Y. Zhang, and T. J. R. Hughes. Isogeometric fluid-structure interaction analysis with applications to arterial blood flow. *Computational Mechanics*, 38:310–322, 2006.

[4] Y. Bazilevs, V.M. Calo, J.A. Cottrell, T.J.R. Hughes, A. Reali, and G. Scovazzi. Variational multiscale residual-based turbulence modeling for large eddy simulation of incompressible flows. *Computer Methods in Applied Mechanics and Engineering*, 197:173–201, 2007.

[5] Y. Bazilevs, L. Beirao da Veiga, J. A. Cottrell, T. J. R. Hughes, and G. Sangalli. Isogeometric analysis: Approximation, stability and error estimates for h-refined meshes. *Mathematical Models and Methods in Applied Sciences*, 16:1031–1090, 2006.

[6] Y. Bazilevs, C. Michler, V.M. Calo, and T.J.R. Hughes. Weak Dirichlet boundary conditions for wall-bounded turbulent flows. *Computer Methods in Applied Mechanics and Engineering*, 196:4853–4862, 2007.

[7] A. N. Brooks and T. J. R. Hughes. Streamline upwind/Petrov-Galerkin formulations for convection dominated flows with particular emphasis on the incompressible Navier-Stokes equations. *Computer Methods in Applied Mechanics and Engineering*, 32:199–259, 1982.

[8] J. Chung and G. M. Hulbert. A time integration algorithm for structural dynamics with improved numerical dissipation: The generalized-α method. *Journal of Applied Mechanics*, 60:371–75, 1993.

[9] J. A. Cottrell, A. Reali, Y. Bazilevs, and T. J. R. Hughes. Isogeometric anal-

ysis of structural vibrations. *Computer Methods in Applied Mechanics and Engineering*, 195:5257–5297, 2006.

[10] T. Elguedj, Y. Bazilevs, V.M. Calo, and T.J.R. Hughes. B-bar and F-bar projection methods for nearly incompressible linear and nonlinear elasticity and plasticity using higher-order NURBS elements. *Computer Methods in Applied Mechanics and Engineering*, 2008. doi:10.1016/j.cma.2008.01.012.

[11] C. Farhat, P. Geuzaine, and C. Grandmont. The discrete geometric conservation law and the nonlinear stability of ALE schemes for the solution of flow problems on moving grids. *Journal of Computational Physics*, 174(2):669–694, 2001.

[12] A. Figueroa, I.E. Vignon-Clementel, K.E. Jansen, T.J.R. Hughes, and C.A. Taylor. A coupled momentum method for modeling blood flow in three-dimensional deformable arteries. *Computer Methods in Applied Mechanics and Engineering*, 195:5685–5706, 2006.

[13] L. Formaggia and F. Nobile. Stability analysis of second-order time accurate schemes for ALE-FEM. *Computer Methods in Applied Mechanics and Engineering*, 193:4097–4116, 2005.

[14] S. Glagov, C. Zarins, D. P. Giddens, and D. N. Ku. Hemodynamics and atherosclerosis: insights and perspectives gained from studies of human arteries. *Archives of Pathology and Laboratory Medicine*, 112:1018–1031, 1988.

[15] J. R. Gohean. A closed-loop multi-scale model of the cardiovascular system for evaluation of ventricular devices. Master's thesis, University of Texas, Austin, May 2007.

[16] G. H. Golub and C. F. Van Loan. *Matrix Computations*. The Johns Hopkins University Press, 1996.

[17] P. L. Gould. *Introduction to Linear Elasticity*. Springer Verlag, Berlin, 1999.

[18] R. Hetzer, M. J. Jurmann, E. V. Potapov, E. Hennig, B. Stiller, J. H. Muller, and Y. Weng. Heart assist systems: current status. *Hertz*, 20:407, 2002.

[19] J.G. Heywood, R. Rannacher, and S. Turek. Artificial boundaries and flux and pressure conditions for the incompressible Navier-Stokes equations. *International Journal of Numerical Methods in Fluids*, 22:325–352, 1996.

[20] G.A. Holzapfel. *Nonlinear Solid Mechanics, a Continuum Approach for Engineering*. Wiley, Chichester, 2000.

[21] T. J. R. Hughes. *A study of the one-dimensional theory of arterial pulse propagation*. PhD thesis, University of California, Berkeley, 1974.

[22] T. J. R. Hughes, J. A. Cottrell, and Y. Bazilevs. Isogeometric analysis: CAD, finite elements, NURBS, exact geometry, and mesh refinement. *Computer Methods in Applied Mechanics and Engineering*, 194:4135–4195, 2005.

[23] T. J. R. Hughes and J. Lubliner. On the one-dimensional theory of blood flow in the large vessels. *Mathematical Biosciences*, 18:161–170, 1973.

[24] K. E. Jansen, C. H. Whiting, and G. M. Hulbert. A generalized-α method for integrating the filtered Navier-Stokes equations with a stabilized finite element method. *Computer Methods in Applied Mechanics and Engineering*, 190:305–319, 1999.

[25] C. Johnson. *Numerical solution of partial differential equations by the finite*

element method. Cambridge University Press, Sweden, 1987.

[26] B. Kar, R. M. Delgado III, O. H. Frazier, I. Gregoric, M. T. Harting, Y. Wadia, T. Myers, R. Moser, and J. Freund. The effect of LVAD aortic outflow-graft placement on hemodynamics and flow. *Journal of the Texas Heart Institute*, 32:294–298, 2005.

[27] P. J. Kilner, G. Z. Yang, R. H. Mohiaddin, D. N. Firmin, and D. B. Longmore. Helical and retrograde secondary flow patterns in the aortic arch studied by three-directional magnetic resonance velocity mapping. *Circulation*, 88:2235–2247, 1993.

[28] P. Le Tallec and J. Mouro. Fluid structure interaction with large structural displacements. *Computer Methods in Applied Mechanics and Engineering*, 190:3039–3068, 2001.

[29] M. J. Levesque, D. Liepsch, S. Moravec, and R.M. Nerem. Correlation of endothelial cell shape and wall shear stress in a stenosed dog aorta. *Arteriosclerosis*, 6:220–229, 1986.

[30] M. J. Levesque and R.M. Nerem. The elongation and orientation of cultured endothelial cells in response to shear stress. *Journal of Biomechanical Engineering*, 107:341–347, 1985.

[31] J. Lighthill. *Mathematical Biofluddynamics, 3rd ed.* SIAM, Philadelphia, PA, 1989.

[32] S. Q. Liu, L. Zhong, and J. Goldman. Control of the shape of a thrombus-neointima-like structure by blood shear stress. *Journal of Biomechanical Engineering*, 124:30, 2002.

[33] J.E. Marsden and T.J.R. Hughes. *Mathematical Foundations of Elasticity*. Dover Publications Inc., New York, 1993.

[34] A. Masud and T. J. R. Hughes. A space-time Galerkin/least-squares finite element formulation of the navier-stokes equations for moving domain problems. *Computer Methods in Applied Mechanics and Engineering*, 148:91–126, 1997.

[35] M. Okano and Y. Yoshida. Junction complexes of endothelial cells in atherosclerosis-prone and atherosclerosis-resistant regions on flow dividers of brachiocephalic bifurcations in the rabbit aorta. *Biorheology*, 31:155–161, 1994.

[36] M. Olufsen. Structured tree outflow condition for blood flow in larger systemic arteries. *American Journal of Physiology*, 276 (1 Pt 2):H257–H268, 1999.

[37] M. Olufsen. A one-dimensional fluid dynamic model of the systemic arteries. *Studies in Health Technology and Informatics*, 71:79–97, 2000.

[38] M. S. Olufsen. *Modeling of the arterial system with reference to an anesthesia simulator*. PhD thesis, Roskilde University, 1998.

[39] Y. Saad and M.H. Schultz. GMRES: A generalized minimal residual algorithm for solving nonsymmetric linear systems. *SIAM Journal of Scientific and Statistical Computing*, 7:856–869, 1986.

[40] A. M. Shaaban and A. J. Duerinckx. Wall shear stress and early atherosclerosis: A review. *American Journal of Roentgenology*, 174:1657–1665, 2000.

[41] J. C. Simo and T. J. R. Hughes. *Computational Inelasticity*. Springer-Verlag, New York, 1998.

[42] K. Stein, T. Tezduyar, and R. Benney. Mesh moving techniques for fluid-structure interactions with large displacements. *Journal of Applied Mechanics*, 70:58–63, 2003.

[43] K. Stein, T.E. Tezduyar, and R. Benney. Automatic mesh update with the solid-extension mesh moving technique. *Computer Methods in Applied Mechanics and Engineering*, 193:2019–2032, 2004.

[44] Texas Advanced Computing Center (TACC). http://www.tacc.utexas.edu.

[45] C. A. Taylor, T. J. R. Hughes, and C. K. Zarins. Finite element modeling of blood flow in arteries. *Computer Methods in Applied Mechanics and Engineering*, 158:155–196, 1998.

[46] C. A. Taylor, T. J. R. Hughes, and C. K. Zarins. Finite element modeling of three-dimensional pulsatile flow in the abdominal aorta: relevance to atherosclerosis. *Annals of Biomedical Engineering*, 26:975–987, 1998.

[47] C. A. Taylor, T. J. R. Hughes, and C. K. Zarins. Effect of exercise on hemodynamic conditions in the abdominal aorta. *Journal of Vascular Surgery*, 29:1077–1089, 1999.

[48] Tayfun E. Tezduyar and Sunil Sathe. Modelling of fluid-structure interactions with the space-time finite elements: Solution techniques. *International Journal of Numerical Methods in Fluids*, 54:855–900, 2007.

[49] Tayfun E. Tezduyar, Sunil Sathe, Timothy Cragin, Bryan Nanna, Brian S. Conklin, Jason Pausewang, and Matthew Schwaab. Modelling of fluid-structure interactions with the space-time finite elements: Arterial fluid mechanics. *International Journal of Numerical Methods in Fluids*, 54:901–922, 2007.

[50] T.E. Tezduyar, M. Behr, S. Mittal, and A.A. Johnson. Computation of unsteady incompressible flows with the stabilized finite element methods – space-time formulations, iterative strategies and massively parallel implementations. In *New Methods in Transient Analysis*, PVP-Vol. 246/ AMD-Vol. 143, pages 7–24. ASME, New York, 1992.

[51] T.E. Tezduyar, S. Sathe, R. Keedy, and K. Stein. Space-time finite element techniques for computation of fluid-structure interactions. *Computer Methods in Applied Mechanics and Engineering*, 195:2002–2027, 2006.

[52] I.E. Vignon-Clementel, C.A. Figueroa, K.E. Jansen, and C.A. Taylor. Outflow boundary conditions for three-dimensional finite element modeling of blood flow and pressure in arteries. *Computer Methods in Applied Mechanics and Engineering*, 195:3776–3796, 2006.

[53] D. M. Wootton and D. N. Ku. Fluid mechanics of vascular systems, diseases, and thrombosis. *Annual Review of Biomedical Engineering*, 1:299, 1999.

[54] Y. Zhang, Y. Bazilevs, S. Goswami, C. Bajaj, and T. J. R. Hughes. Patient-specific vascular NURBS modeling for isogeometric analysis of blood flow. *Computer Methods in Applied Mechanics and Engineering*, 196:2943–2959, 2007.